Quantitative analysis of grain boundary properties in a generalized phase field model for grain growth in anisotropic systems

N. Moelans,* B. Blanpain, and P. Wollants
Department of Metallurgy and Materials Engineering, Katholieke Universiteit Leuven, Kasteelpark Arenberg 44-bus 2450, 3001 Leuven, Belgium

(Received 16 February 2008; revised manuscript received 6 May 2008; published 16 July 2008)

A good choice of model formulation and model parameters is one of the most important and difficult aspects in mesoscale modeling and requires a systematic and quantitative analysis. In this paper, it is studied how the model parameters of a generalized phase field model affect the landscape of the free-energy density functional, the phase field profiles at the grain boundaries, and the corresponding trajectory along the free-energy landscape. The analysis results in quantitative relations between the model parameters, on one hand, and grain boundary energy and mobility, on the other hand. Based on these findings, a procedure is derived that generates a suitable set of model parameters that reproduces accurately a material's grain boundary energy and mobility for arbitrary misorientation and inclination dependence. The misorientation and inclination dependence are formulated so that the diffuse interface width is constant, resulting in uniform stability and accuracy conditions for the numerical solution. The proposed model formulation and parameter choice allow us to perform quantitative simulations with excellent controllability of the numerical accuracy and therefore of the material behavior.

DOI: 10.1103/PhysRevB.78.024113 PACS number(s): 81.40.Ef, 81.30.Hd, 81.05.Bx, 87.16.A−

I. INTRODUCTION

Simulation techniques that describe microstructural evolution on a mesoscale, such as the phase field method, are very important in grain growth studies. When grain boundary energy and mobility are known from experiments,[1] atomistic simulations,[2–4] or theory,[5] mesoscale simulations allow to predict the evolution of the grain size and grain orientation distributions of a given grain structure. They have been extremely valuable in the validation of mean-field theories, for instance, for ideal grain growth[6–9] and grain growth in the presence of second-phase particles.[10–15] Currently, much attention is also given to the evolution of structures in which grain boundary energy and mobility depend on the misorientation between neighboring grains and the grain boundary inclination.[2,16,17] Mesoscale simulations allow us to distinguish between the effects caused by anisotropy in grain boundary energy and those caused by anisotropy in grain boundary mobility.[18,19] The misorientation dependence of grain boundary properties could also play an important role in the nucleation of abnormal grain growth and recrystallization.[20,21] It is, however, still a great challenge to derive reliable conclusions from mesoscale grain growth simulations.

One of the difficulties in mesoscale modeling is that material properties that follow from processes and interactions on the atomistic scale must be introduced into the model in a phenomenological way. In mesoscale models, the properties of a system are usually described by parameterized expressions and the evolution equations are derived based on thermodynamic principles. The phenomenological parameters are related to material properties relevant for the considered process, such as grain boundary energy and mobility in the case of grain growth. Ideally, the phenomenological description captures the important physics and is free from nonphysical side effects. It is also a good modeling approach to reduce the number of model parameters as much as possible. Still, the choice of the phenomenological expressions and model parameters is somehow arbitrary. There may be different mesoscale descriptions for the same physical processes and phenomena. Furthermore, material properties, such as grain boundary energy and mobility, are not always explicit parameters in the phenomenological model; they can be a complicated function of the model parameters. Sometimes, a number of model parameters are also added for numerical or other practical reasons.

The phase field method is a very general technique for modeling complex morphological processes on a mesoscale, such as solidification, precipitation, and grain growth.[22–24] In phase field models, microstructures are represented by order parameter or phase fields that are continuous functions of the spatial coordinates and time. Grain boundaries are implicitly given by narrow regions where the phase fields change smoothly between their values in the neighboring grains. The grain boundary energy is given by an integral of the local free-energy density across this diffuse grain boundary region,[25] which is, however, mostly too complicated to work out analytically, especially when more than one phase field variable must be considered.[26,27] Moreover, due to limitations in computational power, one is usually forced to take the diffuse interface regions in the simulations wider than the physical grain boundary width, in order to perform simulations for relevant length and time scales. The diffuse interface width is then treated as a numerical parameter that determines the accuracy of the simulation results. To account quantitatively for the effect of heat and mass diffusion on solidification and phase transformations, alternative phase field models, often referred to as "thin-interface" models, have been proposed[28–33] that allow us to adjust the diffuse interface width for numerical convenience without affecting the physical grain boundary properties. With respect to systems with nonuniform grain boundary properties, Kazaryan

et al.[34] and Ma *et al.*[35] pointed out that it is important that the model formulation has enough degrees of freedom to vary the grain boundary properties while the diffuse interface width is kept constant.In this way the movement of all grain boundary segments is described with equal accuracy in numerical simulations. Their methodology to determine the model parameters is, however, only approximate[36] or only applicable to two-grain or two-phase structures. Since a large number of phase field variables and model parameters have to be considered for multigrain structures with nonuniform grain boundary properties, it is not straightforward to formulate an appropriate free-energy functional and choose a good set of model parameters that reproduce accurately the desired grain boundary properties. A systematic insight into the effect of each model parameter and the shape of the free-energy functional on the grain boundary properties and the diffuse interface width is consequently required. Furthermore, if the role of each model parameter is understood, it becomes possible to derive indirectly difficult-to-measure material properties, such as grain boundary energy and mobility by comparing mesoscale simulation images with experimental microscope images.

Recently, we introduced an improved phase field formulation for grain growth that is able to account accurately for arbitrary misorientation and inclination dependence of the grain boundary properties.[36] In this paper, we derive quantitative relations between the model parameters and the grain boundary properties for this generalized phase field model. The analysis results in a procedure for calculating an appropriate set of model parameters that reproduces given grain boundary energies and mobilities as a function of misorientation and grain boundary inclination, and guarantees a constant diffuse interface width. The structure of the paper is as follows: First, we study the effect of the model parameters on the shape of the free-energy landscape and the phase field profiles at an interface in local equilibrium for a two-grain structure and systems with uniform grain boundary properties in Sec. II. This analysis results in quantitative relations for the grain boundary energy, mobility, and width as a function of the model parameters. In Sec. III, the model description and the parameter relations are generalized to multigrain systems with arbitrary inclination and misorientation dependence of the grain boundary energy and mobility. An iterative algorithm is described for calculating the appropriate model parameter values for a given set of discrete grain boundary energies and mobilities (for example, for discrete misorientations) and a constant diffuse grain boundary width. Furthermore, inclination-dependent functions are formulated for the model parameters, which reproduce the inclination dependence of a material's grain boundary energy and mobility and guarantee a constant diffuse grain boundary width for arbitrarily strong anisotropy. Conclusions and further directions are formulated in Sec. IV. Applications of the model are described elsewhere.[36,37]

II. INDIVIDUAL GRAIN BOUNDARIES WITH UNIFORM PROPERTIES

A. Model formulation for systems with uniform grain boundary properties

The considered phase field model[36] is based on the phase field formulation from Fan and Chen,[26] Chen and Yang,[38] and Chen[39] for normal grain growth and that of Kazaryan *et al.*[34,40] for grain growth in anisotropic systems. Some modifications were made to the original formulations, which are essential for a fully quantitative approach or simplify the model formulation and model parameter choice.[36] In this type of phase field models for grain growth, different grain orientations are represented by a large set of nonconserved field variables

$$\eta_1(\mathbf{r},t), \eta_2(\mathbf{r},t), \eta_3(\mathbf{r},t), \ldots, \eta_i(\mathbf{r},t), \ldots \eta_p(\mathbf{r},t).$$

We propose a free-energy functional F of the form

$$F = \int_V f(\eta_1, \ldots, \eta_p, \nabla\eta_1, \ldots, \nabla\eta_p)dV = \int_V \left[mf_0(\eta_1, \eta_2, \ldots, \eta_p) + \frac{\kappa}{2}\sum_{i=1}^{p} (\nabla\eta_i)^2 \right] dV, \quad (1)$$

which is a functional of the phase field variables and their gradients. It is assumed that the molar volume is constant and the system is in thermal equilibrium. The energy gradient coefficient κ is strictly positive, so that gradients of the phase field variables give rise to a positive contribution to the free energy of the system. We propose a homogeneous free energy of the form mf_0 with

$$f_0(\eta_1, \eta_2, \ldots, \eta_p) = \sum_{i=1}^{p} \left(\frac{\eta_i^4}{4} - \frac{\eta_i^2}{2} \right) + \gamma \sum_{i=1}^{p} \sum_{j>i}^{p} \eta_i^2 \eta_j^2 + \frac{1}{4}. \quad (2)$$

It has multiple degenerate minima located at

$$(\eta_1, \eta_2, \ldots, \eta_p) = (\pm 1, 0, \ldots, 0), (0, \pm 1, 0, \ldots, 0), \ldots, (0, \ldots, 0, \pm 1).$$

where $f_0 = f_{0,\min} = 0$ for the different grain orientations. This formulation is slightly different from the original.[38] The number of parameters is reduced by 1 without loss of generality and one of the model parameters (m) is placed in front of the homogeneous free energy, which will result in simpler expressions for the grain boundary properties as a function of the model parameters. Furthermore, a constant term $m/4$ is added so that the homogeneous free energy equals zero within grains. In this way, integral (1) equals the total grain boundary energy present in a system. The evolution of the phase field variables is given by the time-dependent Ginzburg–Landau equations,

$$\frac{\partial \eta_i(\mathbf{r},t)}{\partial t} = -L\frac{\delta F(\eta_1, \eta_2, \ldots, \eta_p)}{\delta \eta_i(\mathbf{r},t)} = -L\left[\frac{\partial f(\eta_1, \eta_2, \ldots, \eta_p)}{\partial \eta_i} - \kappa\nabla^2\eta_i \right], \quad (3)$$

with $i = 1, \ldots, p$ and L is a positive kinetic parameter. According to thermodynamic laws, these equations guarantee a continuous decrease in the total grain boundary energy of the system. For systems with uniform grain boundary properties, the model parameters m, γ, κ, and L are constants. In this section, the phase field profiles across a diffuse grain bound-

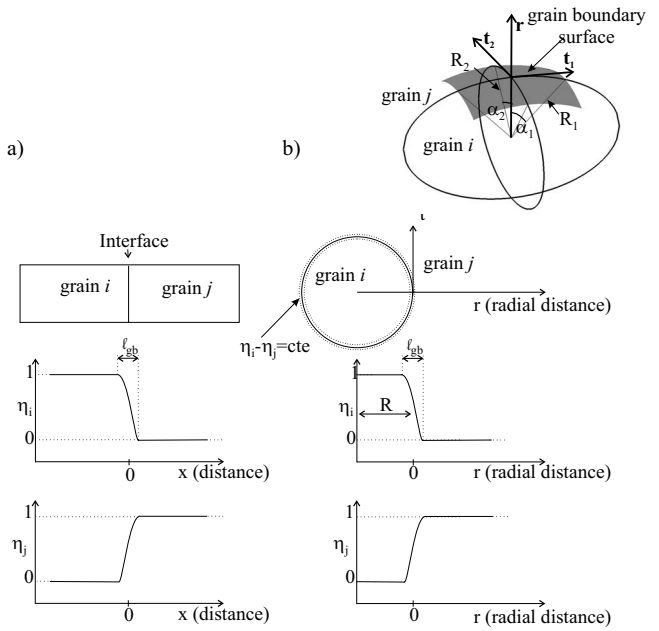

FIG. 1. (a) Phase field representation by means of two phase field variables η_i and η_j of a flat grain boundary between two grains with orientations i and j. ℓ_{gb} is a measure for the width of the diffuse grain boundary region where the phase field variables change between their values in the neighboring grains. (b) Curved grain boundary surface with mean curvatures $1/R_1$ and $1/R_2$ and profiles of the phase field variables along the normal to the grain boundary surface, for a grain with orientation i embedded in a grain with orientation j. A curvilinear coordinate system $\{\mathbf{r},\mathbf{t}_1,\mathbf{t}_2\}$ is indicated, with $\mathbf{r}$ normal to the surface and pointing outward and $\mathbf{t}_1$ and $\mathbf{t}_2$ tangential to the surface. The angles α_1 and α_2 are measured with respect to the $\mathbf{r}$ axis in the $\mathbf{r}$-$\mathbf{t}_1$ and $\mathbf{r}$-$\mathbf{t}_2$ planes, respectively.

ary region and the grain boundary properties are calculated as a function of these model parameters.

B. Equations for a flat interface in equilibrium

To derive equations for the phase field profiles and grain boundary energy of a flat interface in local equilibrium, the two-grain structure shown in Fig. 1(a) with grain orientations i and j and a flat interface at $x=0$ is considered. The grain boundary properties are characterized by parameters m, $\gamma_{i,j}$, and $\kappa_{i,j}$ (where the parameter nomenclature for nonuniform systems is already applied, in which $\gamma_{i,j}$ and $\kappa_{i,j}$ may have different values for different grain boundaries). Following the approach of Cahn and Hilliard[25] and using free-energy functionals given by (1) and (2), the specific grain boundary energy of the system in Fig. 1(a) is given by the integral

$$\sigma_{i,j} = \int_{-\infty}^{+\infty} \left\{ m f_0(\eta_i, \eta_j) + \frac{\kappa_{i,j}}{2} \left[\left(\frac{d\eta_i}{dx} \right)^2 + \left(\frac{d\eta_j}{dx} \right)^2 \right] \right\} dx, \tag{4}$$

where x is the coordinate perpendicular to the grain boundary. For a grain boundary in local equilibrium, the profiles $\eta_i(x)$ and $\eta_j(x)$ adopt a shape that minimizes functional (4) and satisfies the boundary conditions

$$\eta_i = 1 \quad \text{and} \quad \eta_j = 0 \quad \text{for} \quad x \to -\infty, \tag{5a}$$

$$\eta_i = 0 \quad \text{and} \quad \eta_j = 1 \quad \text{for} \quad x \to +\infty, \tag{5b}$$

$$\frac{d\eta_i}{dx} = \frac{d\eta_j}{dx} = 0 \quad \text{for} \quad x \to \pm\infty. \tag{5c}$$

According to the principles of variational calculus,[41,42] the functions $\eta_i(x)$ and $\eta_j(x)$ that extremize functional (4) satisfy

$$m \frac{\partial f_0}{\partial \eta_i} - \kappa_{i,j} \left(\frac{d^2 \eta_i}{dx^2} \right) = 0, \tag{6a}$$

$$m \frac{\partial f_0}{\partial \eta_j} - \kappa_{i,j} \left(\frac{d^2 \eta_j}{dx^2} \right) = 0, \tag{6b}$$

or, equivalently, the integrated equation

$$m f_0 - \frac{\kappa_{i,j}}{2} \left[\left(\frac{d\eta_i}{dx} \right)^2 + \left(\frac{d\eta_j}{dx} \right)^2 \right] = ct = 0, \tag{7}$$

for $\gamma_{i,j}$, $\kappa_{i,j}$, and m constants. Evaluation of the left-hand side of Eq. (7) at $\pm\infty$ and considering boundary conditions (5a)–(5c) gives $ct=0$. Rearrangement of Eq. (7) then yields

$$\frac{d\eta_i}{dx} = -\sqrt{\frac{2mf_0}{\kappa_{i,j}\left[1 + \left(\frac{d\eta_j}{d\eta_i}\right)^2\right]}}, \tag{8a}$$

and

$$\frac{d\eta_j}{dx} = \sqrt{\frac{2mf_0}{\kappa_{i,j}\left[1 + \left(\frac{d\eta_i}{d\eta_j}\right)^2\right]}}, \tag{8b}$$

where boundary conditions (5a)–(5c) are taken into consideration. Combination of Eqs. (4) and (7) gives

$$\sigma_{i,j} = 2m \int_{-\infty}^{+\infty} f_0(\eta_i, \eta_j) dx, \tag{9}$$

and after changing the independent variable from x to η_i using Eq. (8a),

$$\sigma_{i,j} = 2m \int_0^1 f_0(\eta_i, \eta_j(\eta_i)) \frac{dx}{d\eta_i} d\eta_i = \sqrt{2m\kappa_{i,j}} \int_0^1 \sqrt{f_0(\eta_i, \eta_j(\eta_i))} \sqrt{1 + \left(\frac{d\eta_j(\eta_i)}{d\eta_i} \right)^2} d\eta_i, \tag{10}$$

where $\eta_j(\eta_i)$ is the relation between the local values of η_i and η_j along the interfacial profiles across a grain boundary in local equilibrium. It is clear from relation (10) that the grain boundary energy is proportional to the square root of $\kappa_{i,j}$ and m. The remaining integral, however, is in general too complicated to be solved analytically. If Eqs. (6a) and (6b) are combined and the partial derivatives of f_0 are worked out, it follows that

$$\frac{d\left(\frac{d\eta_j}{dx}\right)}{d\left(\frac{d\eta_i}{dx}\right)} = \frac{\eta_j^3 - \eta_j + 2\gamma_{i,j}\eta_i^2\eta_j}{\eta_i^3 - \eta_i + 2\gamma_{i,j}\eta_i\eta_j^2} \tag{11}$$

depends only on the model parameter $\gamma_{i,j}$ and, by consequence, $d\eta_j/d\eta_i$ and $\eta_j(\eta_i)$ do as well. The relation between the specific grain boundary energy and the model parameters can accordingly be written in the form

$$\sigma_{i,j} = g(\gamma_{i,j})\sqrt{\kappa_{i,j}m}. \tag{12}$$

Knowledge of the function $g(\gamma_{i,j})$ and its inverse g^{-1} would greatly facilitate the choice of the model parameters for a given grain boundary energy. Equations (6a) and (6b) for the phase field profiles are evaluated in Sec. II D and integral (10) for the grain boundary energy in Sec. II E. First, the effect of the parameter $\gamma_{i,j}$ on the landscape of the homogeneous free energy is examined.

C. Homogeneous free-energy density landscape

For $\gamma_{i,j} > 0.5$, the combinations of phase field variable values

$$(\eta_i, \eta_j) = (0,0),(\pm 1,0),(0,\pm 1),$$

and

$$\left(\pm\frac{1}{\sqrt{2\gamma_{i,j}+1}}, \pm\frac{1}{\sqrt{2\gamma_{i,j}+1}}\right)$$

satisfy the conditions

$$\frac{\partial f_0}{\partial \eta_i} = \eta_i^3 - \eta_i + 2\gamma_{i,j}\eta_i\eta_j^2 = 0, \tag{13a}$$

$$\frac{\partial f_0}{\partial \eta_j} = \eta_j^3 - \eta_j + 2\gamma_{i,j}\eta_i^2\eta_j = 0, \tag{13b}$$

for the extremal and saddle points of $f_0(\eta_i, \eta_j)$. Only positive values of η_i and η_j will be considered in the further analysis. The point (0,0), where $f_0=0.25$, is a local maximum and the points (1,0), (0,1) are degenerate minima, where $f_0=0$. The point $(\frac{1}{\sqrt{(2\gamma_{i,j}+1)}}, \frac{1}{\sqrt{(2\gamma_{i,j}+1)}})$ is a saddle point. Substitution of $(\eta_i, \eta_j)=(\eta_{\text{saddle}}, \eta_{\text{saddle}})$, with

$$\eta_{\text{saddle}} = \frac{1}{\sqrt{2\gamma_{i,j}+1}}, \tag{14}$$

into Eq. (2) gives

$$f_0(\eta_{\text{saddle}}) = \frac{2\gamma_{i,j}-1}{4(2\gamma_{i,j}+1)}. \tag{15}$$

Both the position and height of the saddle point depend on the model parameter $\gamma_{i,j}$. Furthermore, it follows from conditions (13a) and (13b) that for $\gamma=0.5$, there is an infinite number of minima, namely, all points on the circle $\eta_i^2+\eta_j^2=1$, and for $\gamma_{i,j}<0.5$, the absolute minimum is at $(\frac{1}{\sqrt{(2\gamma_{i,j}+1)}}, \frac{1}{\sqrt{(2\gamma_{i,j}+1)}})$ instead of (0,1) and (1,0). A free energy with $\gamma_{i,j} \leq 0.5$ is thus inappropriate for the description of multigrain structures.

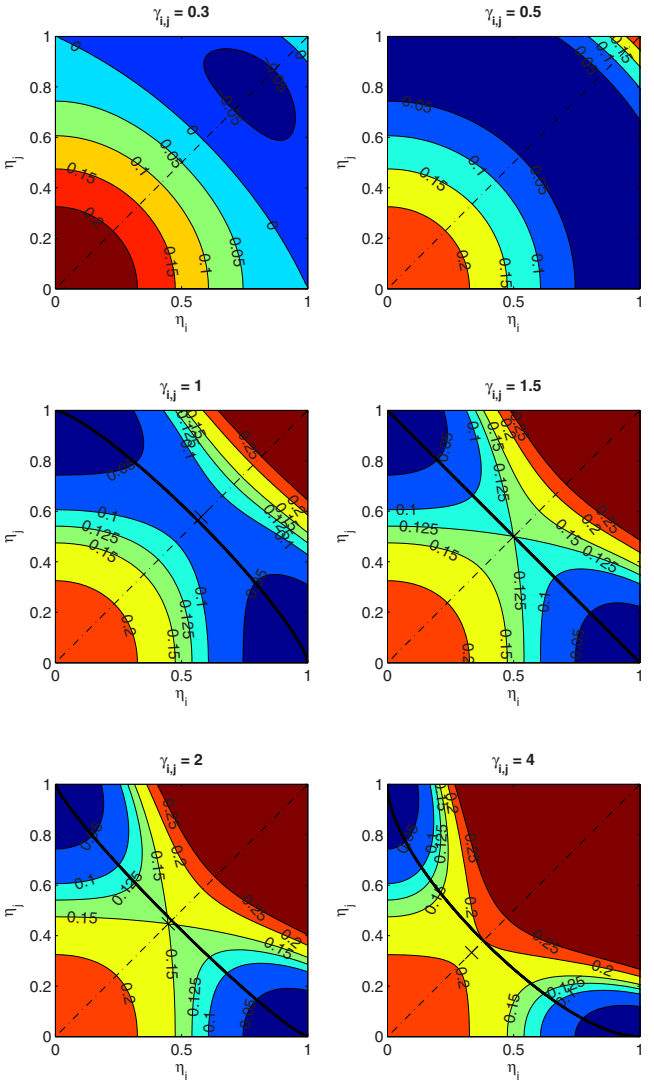

FIG. 2. (Color online) Contour plots of $f_0(\eta_i, \eta_j)$ for different values of the model parameter $\gamma_{i,j}$. The position of the saddle point is indicated with a cross. The dotted line along $\eta_i=\eta_j$ makes clear that the homogeneous free energy is symmetrical with respect to both order parameters. The bold black lines indicate the paths $\eta_j(\eta_i)$ across a grain boundary in local equilibrium.

Figure 2 shows contour plots of the homogeneous free-energy density [Eq. (2)] as a function of two phase field variables η_i and η_j and for different values of $\gamma_{i,j}$. For $\gamma_{i,j} > 0.5$, there are clearly localized minima at (1,0) and (0,1). The saddle points are indicated with a cross. For all values of $\gamma_{i,j}$, the free energy is symmetrical with respect to the diagonal $\eta_i=\eta_j$. It is not symmetrical with respect to the diagonal $\eta_i=1-\eta_j$ since the contribution of the term $\gamma_{i,j}\eta_i^2\eta_j^2$ increases with the values of the phase field variables. Moreover, for larger values of $\gamma_{i,j}$, the contours deviate more toward the corner $(\eta_i, \eta_j)=(0,0)$ and the saddle point is at smaller values of the phase field variables. The relation $\eta_j(\eta_i)$ between the values of the phase field variables along their profiles across a grain boundary in local equilibrium is indicated using a bold line and will be commented on in Sec. II D.

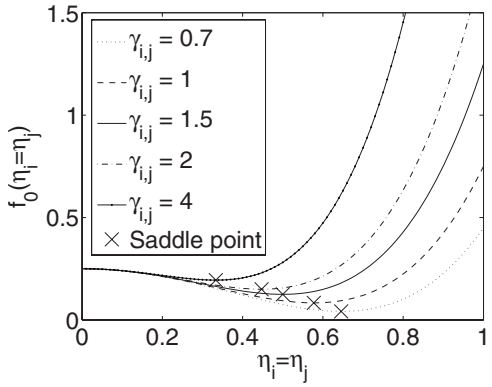

FIG. 3. Evolution of f_0 along the diagonal $\eta_i=\eta_j$ for different values of $\gamma_{i,j}$. The saddle point is indicated with a cross.

The evolution of f_0 along the diagonal $\eta_i=\eta_j$ is plotted for different $\gamma_{i,j}$ in Fig. 3. For all values of $\gamma_{i,j}$, there is a local maximum $f_0=0.25$ at $\eta_i=\eta_j=0$. There would be a minimum at $\eta_i=\eta_j=1$ for $\gamma_{i,j}=0$. However, for $\gamma_{i,j}>0.5$, the contribution $\gamma_{i,j}\eta_i^2\eta_j^2$, which increases as $\eta_1=\eta_2$ approaches 1, prevents the minimum at $\eta_i=\eta_j=1$ and introduces a saddle point [minimum along the curve for $f_0(\eta_i,\eta_j)$]. The function values increase and the saddle point shifts toward smaller values for increasing values of $\gamma_{i,j}$. For $\gamma_{i,j}=1.5$, the saddle point is at $\eta_i=\eta_j=0.5$.

If more phase field variables are considered, the degenerate minima of the homogeneous free energy [Eq. (2)] are located at $(\eta_i=1,\ \eta_{j\neq i}=0)$ and there is a local maximum at $\eta_i=0$, assuming $\gamma>0.5$ and $i,j=1,\ldots,p$. Moreover, there are saddle points at

$$\left(\eta_i=\eta_j=\frac{1}{\sqrt{1+(2-1)\gamma}},\eta_{k\neq i,j}=0\right)$$

for all combinations of two phase field variables and

$$\left(\eta_i=\eta_j=\eta_k=\frac{1}{\sqrt{1+(3-1)\gamma}},\eta_{l\neq i,j,k}=0\right)$$

for all combinations of three phase field variables, etc., for higher-order combinations. Because of the term $\gamma\Sigma_{i<j}\eta_i^2\eta_j^2$, each extra phase field variable with a value different from 0 gives a positive contribution to the local free-energy density. By consequence, within grains only one of the phase field variables differs from 0 (it equals 1); and at grain boundaries and multijunctions, only those phase field variables representing the adjacent grains are different from zero.

D. Interfacial profiles

The equilibrium profiles of η_i and η_j are given by differential equations (6a) and (6b) in combination with boundary conditions (5a)–(5c). In this section, the differential equations are first solved analytically for symmetrical phase field profiles; this is the case for $\gamma_{i,j}=1.5$. Then, numerically calculated profiles are analyzed for the general case.

1. Analytical calculation of symmetrical profiles

In the present study, a "symmetrical profile" refers to a profile for which $\eta(x)=1-\eta(-x)$, assuming that the central plane of the diffuse grain boundary region is located at $x=0$. Since free-energy formulations (1) and (2) are symmetrical with respect to η_i and η_j, the following relations exist for symmetrical phase field profiles $\eta_i(x)$ and $\eta_j(x)$ across a grain boundary in local equilibrium:

$$\eta_j=1-\eta_i, \tag{16a}$$

$$\frac{d\eta_j}{dx}=-\frac{d\eta_i}{dx}, \tag{16b}$$

and

$$\frac{d^2\eta_j}{dx^2}=-\frac{d^2\eta_i}{dx^2}. \tag{16c}$$

Consequently, for symmetrical profiles the path $\eta_i(\eta_j)$ and its inverse are known and have a simple form, namely, relation (16a). Furthermore, it follows from conditions (16a)–(16c) that the profiles of the phase field variables cross at $\eta_i=\eta_j=\eta_{\text{interf}}=0.5$ and that $d\eta_i/d\eta_j=-1$ and $d(d\eta_i/dx)/d(d\eta_j/dx)=-1$ along the profiles. Application of condition (16c) to differential equations (6a) and (6b) gives that the two phase field profiles across a diffuse interface can only be symmetrical if at every point x along the profile

$$\frac{\partial f_0}{\partial\eta_j}=-\frac{\partial f_0}{\partial\eta_i}, \tag{17}$$

or using Eq. (13a) and (13b) for the partial derivatives of f_0 with $\eta_j=1-\eta_i$,

$$-(1+2\gamma_{i,j})\eta_i^3+(3+2\gamma_{i,j})\eta_i^2-2\eta_i=-(1+2\gamma_{i,j})\eta_i^3+4\gamma_{i,j}\eta_i^2-(2\gamma_{i,j}-1)\eta_i. \tag{18}$$

This requirement can only be satisfied at every point along the interface for $\gamma_{i,j}=1,5$.

Since for symmetrical profiles $\eta_j(\eta_i)=1-\eta_i$, it is straightforward to eliminate one of the phase field variables from Eqs. (6a), (6b), (8a), and (8b) for a boundary in local equilibrium. The functional f_0 and its partial derivatives can be written as

$$f_0(\eta_i,1-\eta_i)=\left(\frac{\eta_i^4}{4}-\frac{\eta_i^2}{2}\right)+\left[\frac{(1-\eta_i)^4}{4}-\frac{(1-\eta_i)^2}{2}\right]+\gamma_{i,j}\eta_i^2(1-\eta_i)^2+\frac{1}{4}=\left(\frac{1}{2}+\gamma_{i,j}\right)\eta_i^2(1-\eta_i)^2, \tag{19}$$

and

$$\frac{\partial f_0}{\partial\eta_i}(\eta_i,1-\eta_i)=(1+2\gamma_{i,j})\eta_i^3-4\gamma_{i,j}\eta_i^2+(2\gamma_{i,j}-1)\eta_i. \tag{20}$$

Analogous expressions are obtained for $\partial f_0/\partial\eta_i$ as a function of η_j and $\partial f_0/\partial\eta_j$ as a function of η_i or η_j. As a result, for symmetrical profiles, differential equations (6a) and (6b) become

$$\frac{d^2\eta_i}{dx^2} = \frac{m}{\kappa_{i,j}} 2\eta_i(2\eta_i^2 - 3\eta_i + 2), \tag{21a}$$

$$\frac{d^2\eta_j}{dx^2} = \frac{m}{\kappa_{i,j}} 2\eta_j(2\eta_j^2 - 3\eta_j + 2), \tag{21b}$$

and integrated equations (8a) and (8b)

$$\frac{d\eta_i}{dx} = -\sqrt{\frac{2m}{\kappa_{i,j}}}\eta_i(1-\eta_i), \tag{22a}$$

$$\frac{d\eta_j}{dx} = \sqrt{\frac{2m}{\kappa_{i,j}}}\eta_j(1-\eta_j), \tag{22b}$$

where it is applied that $\gamma_{i,j}=1.5$ and $d\eta_i/d\eta_j = d\eta_j/d\eta_i = -1$. It can be verified that the profiles

$$\eta_i(x) = \frac{1}{2}\left[1 - \tanh\left(\sqrt{\frac{m}{2\kappa_{i,j}}}x\right)\right], \tag{23a}$$

$$\eta_j(x) = \frac{1}{2}\left[1 + \tanh\left(\sqrt{\frac{m}{2\kappa_{i,j}}}x\right)\right], \tag{23b}$$

satisfy Eqs. (21a), (21b), (22a), and (22b) in combination with boundary conditions (5a)–(5c).

2. Numerical calculation of arbitrary profiles

It follows from requirement (18) that, in general, the phase field profiles are not symmetrical except for $\gamma_{i,j}=1.5$. For asymmetrical profiles, the ratios $(d^2\eta_i/dx^2)/(d^2\eta_j/dx^2)$ and $(d\eta_i/dx)/(d\eta_j/dx)$ are not constant along the profiles and the relationship between $\eta_i(x)$ and $\eta_j(x)$ is complex. It was not possible to identify analytical expressions for the profiles $\eta_i(x)$ and $\eta_j(x)$, which satisfy differential equations (6a) and (6b). Therefore, numerical simulations were performed to study the effect of the model parameters m, $\kappa_{i,j}$, and $\gamma_{i,j}$ on the equilibrium shape of the profiles, using the one-dimensional two-grain geometry shown in Fig. 1(a). In the simulations, the phase field profiles evolved toward their equilibrium shape, starting from a sharp transition at the grain boundary. To obtain a well resolved representation of the profiles, an extremely fine grid was used: the grid spacing was 0.1 or smaller, so that there were at least 100 grid points (g.p.) between the positions $x=-5$ and $x=5$ (see Figs. 4 and 7). The distance between the markers on the curves in the figures is many times the grid spacing used in the numerical calculations.

Numerically calculated phase field profiles are shown for different values of $\gamma_{i,j}$ and a constant ratio $\kappa_{i,j}/m$ in Fig. 4(a) and for different ratios $\kappa_{i,j}/m$ and constant $\gamma_{i,j}$ in Fig. 4(b). Comparison of the numerically calculated profiles for $\gamma_{i,j}=1.5$ with analytical profiles (23a) and (23b) indicates that the numerically calculated profiles converge to the analytical solution of Eqs. (6a) and (6b) and that the grid spacing results in well resolved phase field profiles. Since the homogeneous free energy is symmetrical with respect to the phase field variables, the profiles $\eta_i(x)$ and $\eta_j(x)$ are each other's mirror image with respect to the center of the diffuse interface region, where the phase field variables intersect; this means that $\eta_i(x)=\eta_j(-x)$. The value at which the phase field profiles intersect, η_{interf}, depends only on the parameter $\gamma_{i,j}$. This also follows from Eqs. (8a) and (8b) since f_0 and $d\eta_i/d\eta_j$ are a function only of the model parameter $\gamma_{i,j}$, and the parameters $\kappa_{i,j}$ and m are constant along the interfacial profiles. Except for $\gamma_{i,j}=1.5$, the profiles of the phase field variables themselves are not symmetrical and their local sum is not constant along the profiles. Condition (16a) is accord-

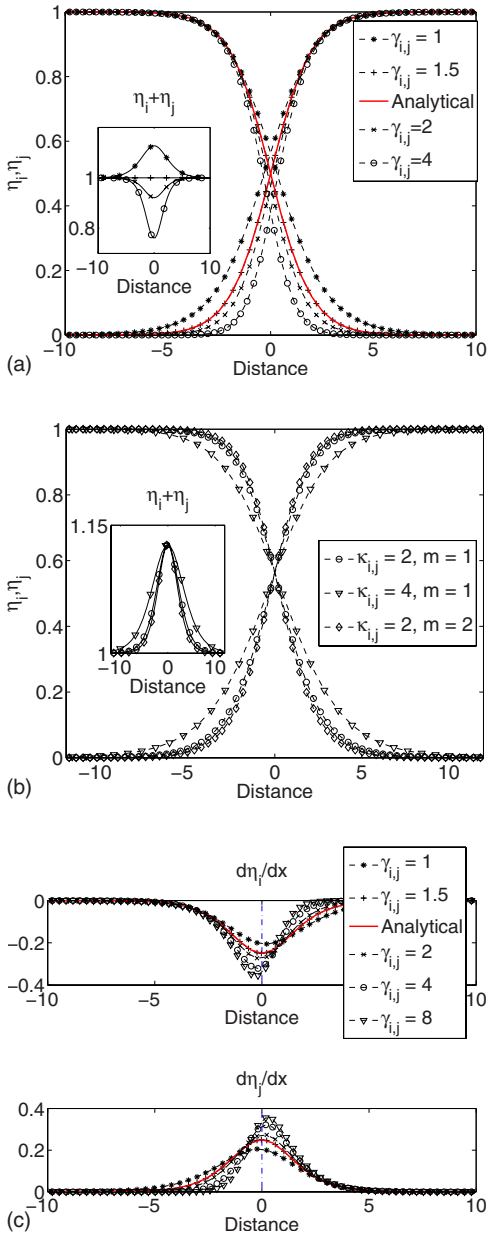

FIG. 4. (Color online) (a) Numerically calculated equilibrium profiles for the phase field variables $\eta_i(x)$ and $\eta_j(x)$ across a grain boundary for $\kappa_{i,j}=2$, $m=1$, and different values for $\gamma_{i,j}$. (b) Numerically calculated equilibrium profiles for the phase field variables $\eta_i(x)$ and $\eta_j(x)$ across a grain boundary for $\gamma_{i,j}=1$ and different combinations of the parameters $\kappa_{i,j}$ and m. (c) Evolution of $d\eta_i/dx$ and $d\eta_j/dx$ along the interfacial profile for $\kappa_{i,j}=2$, $m=1$ and different values for $\gamma_{i,j}$. In (b) and (c), the analytical curves obtained for $\gamma_{i,j}=1.5$ are added.

ingly not satisfied. For fixed $\gamma_{i,j}$ values, the width of the interfacial profiles is proportional to $\sqrt{\kappa_{i,j}/m}$ (see also Sec. II F).

In Fig. 4(c), the gradients of the phase field profiles are plotted as a function of the distance from the middle of the interface for different $\gamma_{i,j}$ values and a constant $m/\kappa_{i,j}$ ratio. For $\gamma_{i,j}=1.5$, the curves are symmetrical with respect to $x=0$ and the local gradients of η_i and η_j are equal in magnitude. By consequence, $d\eta_i/d\eta_j=d\eta_j/d\eta_i=-1$ along the profiles. For $\gamma_{i,j}$ farther from 1.5, the curves become more asymmetric and the local gradients of η_i and η_j differ. At the middle of the interface, however, the gradients of the two profiles are maximal in absolute value and equal in size for all values of $\gamma_{i,j}$, giving $(d\eta_i/d\eta_j)_{\text{interf}}=(d\eta_j/d\eta_i)_{\text{interf}}=-1$. The graphs also show that for a given ratio $m/\kappa_{i,j}$, the maximal gradient at the middle of the interface increases with the value of $\gamma_{i,j}$. For fixed $\gamma_{i,j}$ values, the gradients along the phase field profiles are proportional to $\sqrt{m/\kappa_{i,j}}$ [see relations (8a) and (8b)].

Although the evolution of each phase field variable toward equilibrium is independent, there exists a relation between the local values of the two-phase field variables, which are changing values across a diffuse boundary in local equilibrium. This relation $\eta_j(\eta_i(x))$ [or $\eta_i(\eta_j(x))$] depends on the value of the model parameter $\gamma_{i,j}$ and is plotted for a number of $\gamma_{i,j}$ values in Fig. 5(a). The paths of (η_i, η_j) values across a diffuse grain boundary are also indicated on the free-energy landscapes in Fig. 2. For $\gamma_{i,j}=1.5$, the path corresponds with the diagonal $\eta_j=1-\eta_i$ and goes through the saddle point of the homogeneous free energy at $\eta_i=\eta_j=0.5$. For $\gamma_{i,j}\neq 1.5$, the curves deviate toward the saddle point; however, they do not reach it. Figure 5(b) shows how $d\eta_i/d\eta_j$ varies with the value of one of the phase field variables η_i. Conforming with the results presented in Fig. 4(b), $d\eta_i/d\eta_j$ may vary between 0 and $-\infty$, but equals -1 at $x=0$ for all values of $\gamma_{i,j}$. For symmetrical profiles, $d\eta_i/d\eta_j$ is constant and equal to -1 along the whole profile.

In Fig. 6(a), the value at which the phase field variables cross, η_{interf}, is compared with the coordinates of the saddle point of the homogeneous free energy η_{saddle} for a large range of $\gamma_{i,j}$ values. The difference between η_{interf} and η_{saddle} is relatively small for $\gamma_{i,j}$, between 0.5 and 2, and increases drastically for larger values of $\gamma_{i,j}$. For $\gamma_{i,j}=1.5$, η_{interf} equals η_{saddle}; and for $\gamma_{i,j}\to 0.5$, $\eta_{\text{interf}}\to\eta_{\text{saddle}}=1/\sqrt{2}$, which is calculated from Eq. (14) with $\gamma_{i,j}=0.5$.

E. Grain boundary energy

In diffuse interface models, the excess energy associated with a grain boundary is smeared out over the diffuse grain boundary region. Integration of the excess energy along the phase field profiles gives the specific grain boundary energy, which is a measurable quantity.

1. Spatial distribution of the excess energy

The integrant in Eq. (4) gives the local excess energy density due to the presence of a grain boundary, which consists of a homogeneous contribution, mf_0, and a gradient contribution, $0.5\kappa_{i,j}[(d\eta_i/dx)^2+(d\eta_j/dx)^2]$. It follows from

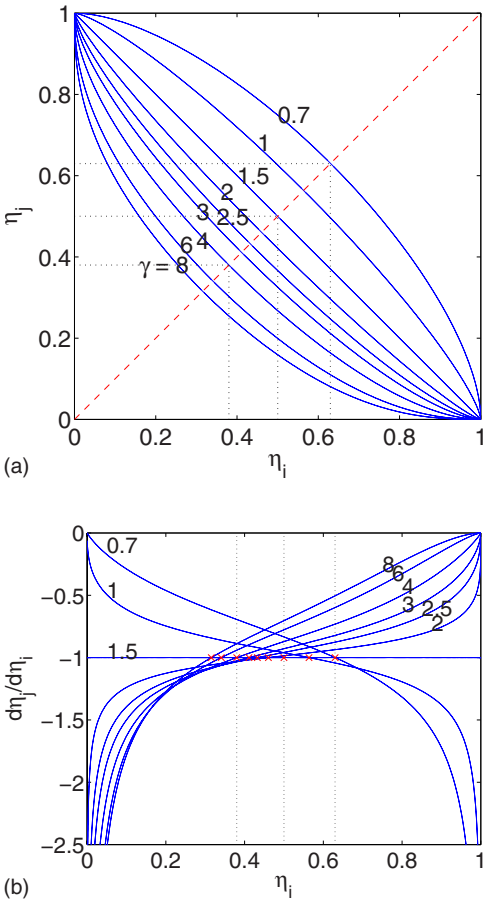

FIG. 5. (Color online) Variation of (a) η_j and (b) $d\eta_j/d\eta_i$ as a function of η_i along equilibrium phase field profiles across a grain boundary, obtained from numerical simulations for different values of the parameter $\gamma_{i,j}$ (curves for $d\eta_i/d\eta_j$ as a function of η_j are identical). The intersections of the diagonal line (red) for $\eta_i=\eta_j$ with the $\eta_j(\eta_i)$ curves give the values at which the phase field profiles cross at the center of the diffuse grain boundary region. For the different values of $\gamma_{i,j}$, η_{interf} is indicated with a (red) cross.

relation (7) that both contributions are equal at every position along the profiles.

For $\gamma_{i,j}=1.5$, the energy density curves can be calculated analytically from Eqs. (19), (23a), and (23b), giving

$$mf_0(\eta_i(x),\eta_j(x)) = 2m\eta_i^2(1-\eta_i)^2 = \frac{m}{8}\left[\cosh\left(\sqrt{\frac{m}{2\kappa_{i,j}}}x\right)\right]^{-4}, \tag{24}$$

for the homogeneous energy density and

$$\frac{\kappa_{i,j}}{2}\left[\left(\frac{d\eta_i}{dx}\right)^2+\left(\frac{d\eta_j}{dx}\right)^2\right] = \kappa_{i,j}\left(\frac{d\eta_i}{dx}\right)^2 = \frac{m}{8}\left[\cosh\left(\sqrt{\frac{m}{2\kappa_{i,j}}}x\right)\right]^{-4} \tag{25}$$

for the gradient energy density. The spatial distribution of the excess energy density due to the presence of a grain bound-

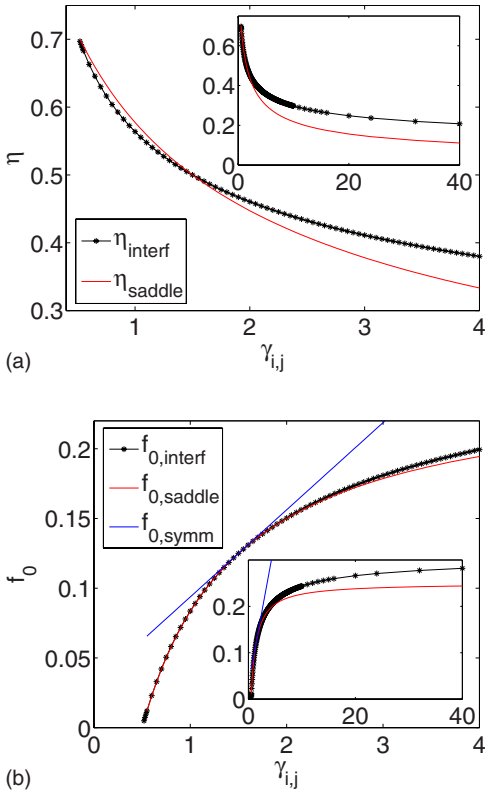

FIG. 6. (Color online) η_{interf} as a function of $\gamma_{i,j}$, obtained from numerical simulations, compared with analytical relation (14) for $\eta_{\text{saddle}}(\gamma_{i,j})$. (b) $f_{0,\text{interf}}$ as a function of $\gamma_{i,j}$, obtained from numerical simulations, compared with relation (15) for $f_{0,\text{saddle}}(\gamma_{i,j})$ and relation (19) for $f_{0,\text{symm}}(\gamma_{i,j})$, evaluated for different values of $\gamma_{i,j}$. The latter assumes that the profiles are symmetrical and intersect at $\eta_i = \eta_j = 0.5$.

ary is given by the sum of both terms. The curves reach a maximum at the middle of the interface, where $f_{0,\text{interf}} = m/8$.

For arbitrary profiles ($\gamma_{i,j} \neq 1.5$), the free-energy curves and their maximum at the middle of the diffuse grain boundary region were calculated numerically for the equilibrium phase field profiles described in Sec. II D. The spatial variation of the homogeneous and gradient contributions in the energy density are plotted in Figs. 7(a) and 7(b) for different values of the model parameters $\gamma_{i,j}$, $\kappa_{i,j}$, and m. For all parameter values, the curves are symmetrical and have a maximum at the middle of the profile. The major contribution to the grain boundary energy is concentrated near the center of the diffuse grain boundary region. Comparison of Figs. 7(a) and 7(b) with Figs. 4(a) and 4(b) reveals that the tails of the energy density peak are much shorter than those of the profiles of the phase field variables. For constant $\kappa_{i,j}$ and m, the maximum of the curves increases with increasing $\gamma_{i,j}$. For constant $\gamma_{i,j}$, the height of the peak is proportional to m, whereas $\kappa_{i,j}$ has no effect on the height. Since the phase field profiles are wider for larger values of the ratio κ/m, a larger value for κ/m accordingly results in a wider energy density peak in Fig. 7(b).

The evolution of f_0 across a diffuse grain boundary as a function of one of the phase field variables is plotted for

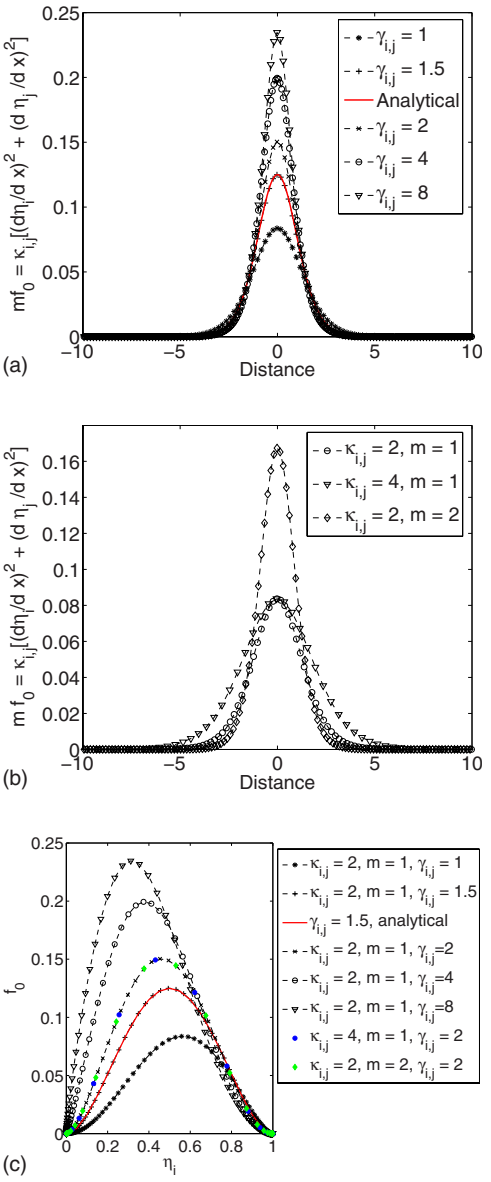

FIG. 7. (Color online) (a) Profiles of the homogeneous and gradient energy density variations across a grain boundary for $\kappa_{i,j}=2$, $m=1$ and different values of $\gamma_{i,j}$. The analytical relations for $\gamma_{i,j}=1.5$ are added. (b) Profiles of the energy density variations across a grain boundary for $\gamma_{i,j}=1$ and different combinations of the values of $\kappa_{i,j}=4$, $m=1$. (c) Evolution of f_0 along numerically calculated paths for $\eta_j(\eta_i)$. The curves were obtained for $\kappa_{i,j}=2$, $m=1$ and different values of $\gamma_{i,j}$. A number of points, obtained for $\kappa_{i,j}=4$, $m=1$ and $\kappa_{i,j}=2$, $m=2$ with $\gamma_{i,j}=2$ are added.

different values of $\gamma_{i,j}$ in Fig. 7(c). The maximum of the curve is always located at $\eta_i = \eta_{\text{interf}}$. The extra points for various values of $\kappa_{i,j}$ and m on the curve for $\gamma_{i,j}=2$ show that the paths $(\eta_i, \eta_j(\eta_i))$ and $(\eta_i, f_0(\eta_i, \eta_j(\eta_i)))$ across a diffuse grain boundary depend only on the model parameter $\gamma_{i,j}$.

The gradients of the phase field profiles are proportional to the square root of the local value of the homogeneous energy density [see Eq. (8a) and (8b)]. By consequence, the maximum of f_0 along the profiles determines the stability and accuracy conditions for the numerical solution of the phase field equations. The value of f_0 at the middle of the

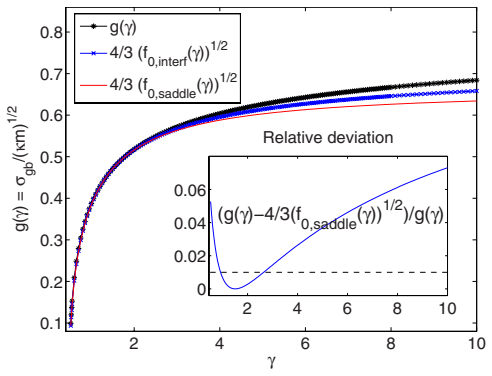

FIG. 8. (Color online) Numerically calculated function values of $g(\gamma_{i,j})=\sigma_{i,j}/\sqrt{\kappa_{i,j}m}$ and numerically calculated values of $4/3\sqrt{f_{0,\mathrm{interf}}(\gamma_{i,j})}$ for a large number of $\gamma_{i,j}$ values, together with analytical relation (15) for $4/3\sqrt{f_{0,\mathrm{saddle}}(\gamma_{i,j})}$. The relative deviation between $g(\gamma_{i,j})$ and $4/3\sqrt{f_{0,\mathrm{saddle}}(\gamma_{i,j})}$ is also shown as a function of $\gamma_{i,j}$.

diffuse interface region, $f_{0,\mathrm{interf}}=f_0(\eta_{\mathrm{interf}},\eta_{\mathrm{interf}})$, was obtained for a large range of $\gamma_{i,j}$ values from the numerically calculated profiles. The data points are plotted in Fig. 6(b) and compared with analytical relation (15) for $f_{0,\mathrm{saddle}}(\gamma_{i,j})$ and analytical relation (19) for $f_{0,\mathrm{symm}}(\gamma_{i,j})$. As shown in Figs. 2 and 6(a), the path $\eta_j(\eta_i)$ across an interface in equilibrium does not reach the saddle point of f_0 except for $\gamma_{i,j}=1.5$. By consequence, the numerically determined values for $f_{0,\mathrm{interf}}$ differ from $f_{0,\mathrm{saddle}}$, although the deviation is very small for $\gamma_{i,j}$ smaller than 2.5; see Fig. 8 for a quantitative evaluation of the relative deviation. For larger values of $\gamma_{i,j}$, the curves for $f_{0,\mathrm{interf}}$ and $f_{0,\mathrm{saddle}}$ diverge. The line for $f_{0,\mathrm{symm}}$ [Fig. 6(b)] was obtained by evaluating Eq. (19) for symmetrical interfaces, at $\eta_i=0.5$ and as a function of $\gamma_{i,j}$. It gives the maximum of f_0 along the diagonal $\eta_j=1-\eta_i$ for different values of $\gamma_{i,j}$. This curve reveals that the assumption of a symmetrical interface with $\eta_j=1-\eta_i$, and accordingly $\eta_{\mathrm{interf}}=0.5$, cannot give a good approximation for $f_{0,\mathrm{interf}}$, the diffuse grain boundary width or the specific grain boundary energy.

2. Specific grain boundary energy

For symmetrical profiles, substitution of Eqs. (16b) and (19) into Eq. (10) gives

$$\sigma_{i,j}=2\sqrt{m\kappa_{i,j}\left(\frac{1}{2}+\gamma_{i,j}\right)}\int_0^1\eta_i(1-\eta_i)d\eta_i$$

$$=\frac{1}{3}\sqrt{m\kappa_{i,j}\left(\frac{1}{2}+\gamma_{i,j}\right)} \tag{26}$$

$$=\frac{\sqrt{2}}{3}\sqrt{m\kappa_{i,j}}, \tag{27}$$

for the specific grain boundary energy. The function $g(\gamma_{i,j})$, introduced in Eq. (12), accordingly equals $\sqrt{2}/3$ for $\gamma_{i,j}=1.5$. Furthermore, since for symmetrical interfaces $f_{0,\mathrm{interf}}=f_{0,\mathrm{saddle}}=1/8$, $g(\gamma_{i,j})=\frac{4}{3}\sqrt{f_{0,\mathrm{interf}}(\gamma_{i,j})}=\frac{4}{3}\sqrt{f_{0,\mathrm{saddle}}(\gamma_{i,j})}$.

To characterize the function $g(\gamma_{i,j})=\sigma_{i,j}/\sqrt{\kappa_{i,j}m}$, the integral expression of the specific grain boundary energy [Eq. (4)] was numerically evaluated for a large number of $\gamma_{i,j}$ values between 0.52 and 40 using an interspacing $\Delta\gamma_{i,j}\leq 0.05$. Calculated function values are plotted as a function of $\gamma_{i,j}$ in Fig. 8 and compared with numerically calculated values for $4/3\sqrt{f_{0,\mathrm{interf}}(\gamma_{i,j})}$ and with the analytical curve $4/3\sqrt{f_{0,\mathrm{saddle}}(\gamma_{i,j})}$ obtained from Eq. (15). The figure shows that the three relations coincide for $\gamma_{i,j}=1.5$ and that for nearly symmetrical interfaces, the analytical equation $4/3\sqrt{f_{0,\mathrm{saddle}}(\gamma_{i,j})}$ is a good approximation for the functions $g(\gamma_{i,j})$ and $4/3\sqrt{f_{0,\mathrm{interf}}(\gamma_{i,j})}$. For $\gamma_{i,j}$ within the range [0.9 2.65], the relative error is smaller than 1%, which is much smaller than the scatter on experimental data for grain boundary energies and mobilities, or the usual discretization errors on the numerical solution of the phase field equations; the relative error is smaller than 2% for $\gamma_{i,j}$ in the range [0.75 3.45] and smaller than 5% for $\gamma_{i,j}$ in the range [0.53 6.5].

Mostly,[34,43,44] it is assumed that the grain boundary width is proportional to $\sqrt{\kappa/(\Delta f)_{\max}}$ and the specific grain boundary energy with $\sqrt{\kappa(\Delta f)_{\max}}$, where $(\Delta f)_{\max}$ is defined as the maximum height of the barrier in the homogeneous free-energy density f between two degenerate minima, although it has never been specified how this value is determined. It is not clear whether it corresponds with the $f_{0,\mathrm{interf}}$ or $f_{0,\mathrm{saddle}}$ used in this paper. Nevertheless, the numerically calculated curves for $g(\gamma_{i,j})$ and $f_{0,\mathrm{interf}}(\gamma_{i,j})$ show that such an approach is not fully quantitative for large variations in grain boundary energy (see also Sec. III B).

F. Diffuse grain boundary width

In phase field simulations for grain growth, the width of the diffuse grain boundaries is most often chosen based on computational considerations. To increase the length and time scale of the simulations, it is taken larger than the physical grain boundary thickness, but still several orders smaller than the mean grain size. Since, strictly spoken, the diffuse interface thickness reaches infinity, there are many possibilities to define a measure for the grain boundary width. For further analysis, we propose a definition that is based on the absolute value of the gradients of the phase field profiles at $x=0$:

$$\ell_{\mathrm{gb}}=\frac{1}{|(d\eta_i/dx)_{x=0}|}$$

$$=\frac{1}{|(d\eta_j/dx)_{x=0}|}=\sqrt{\frac{\kappa_{i,j}}{mf_{0,\mathrm{interf}}}}, \tag{28}$$

which is obtained from Eqs. (8a) and (8b) evaluated at $x=0$, where $d\eta_i/d\eta_j=-1$ and $f_0=f_{0,\mathrm{interf}}$. Since the profiles are steepest at the middle of the diffuse grain boundary region, a grain boundary width defined in this way can be used in numerical criteria for stability and accuracy.

Evaluation of expression (28) for symmetrical interfaces using Eq. (22a) and (22b) with $f_0(1/2,1/2)=1/8$ or derivatives (23a) and (23b) gives

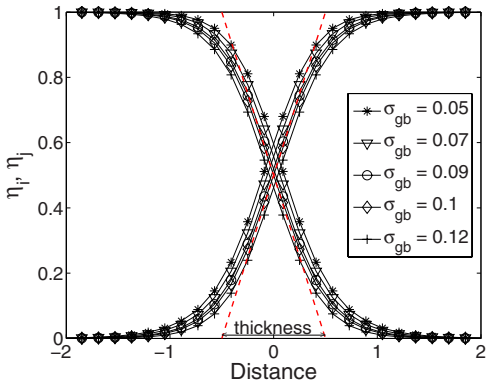

FIG. 9. (Color online) Profiles of the phase field variables for grain boundaries with different grain boundary energies and equal diffuse grain boundary width, according to definition (28). The parameter values m=0.6; γ=0.8262, 1.0336, 1.3156, 1.4976, and 1.9838; and κ=0.0371, 0.0523, 0.0675, 0.0750, and 0.0898 were used in order to obtain a grain boundary width ℓ_{gb}=1 and grain boundary energies σ_{gb}=0.05, 0.07, 0.09, 0.1, and 0.12, The dotted lines give a graphical interpretation of definition (28).

$$\ell_{gb} = \sqrt{\frac{8\kappa_{i,j}}{m}}. \tag{29}$$

For asymmetrical profiles, the value of $f_{0,\text{interf}}$ must be calculated numerically as a function of $\gamma_{i,j}$. As shown in Fig. 6(b), $f_{0,\text{interf}}(\gamma_{i,j})$ is approximated very well by analytical relation (15) for $\gamma_{i,j}$ not too far from 1.5.

In Fig. 9, phase field profiles are shown for grain boundaries with different grain boundary energies, but equal width according to definition (28). All profiles have the same gradient at the center of the diffuse grain boundary region. The dotted lines give a graphical interpretation of the definition of ℓ_{gb}. The lines pass through the point (0,0.5) and are parallel with the tangent to the phase field profiles at x=0. Then, the grain boundary width equals the distance between the two intersections of these lines with the x axis.

G. Grain boundary velocity

Mostly,[45–48] the velocity of curved interfaces in phase field models is derived for sharp interface conditions, where it is assumed that the width ℓ_{gb} of the grain boundary is much smaller than its radii of curvature, R_1 and R_2. Consider thereto a grain with orientation i embedded in another grain with orientation j, as illustrated in Fig. 1(b). Furthermore, for every point on the grain boundary surface a curvilinear coordinate system $(\mathbf{r},\mathbf{t}_1,\mathbf{t}_2)$ is defined with $\mathbf{r}$ pointing outward in the direction of the normal to the surface and $\mathbf{t}_1$ and $\mathbf{t}_2$ tangential to the surface. Reformulation of evolution equation (3) for the curvilinear coordinate system gives[45,46]

$$\frac{\partial \eta_i}{\partial t} = -L_{i,j}\left\{ m\frac{\partial f_0}{\partial \eta_i} - \kappa_{i,j}\left[\frac{\partial^2 \eta_i}{\partial r^2} + \left(\frac{1}{R_1}+\frac{1}{R_2}\right)\frac{\partial \eta_i}{\partial r}\right]\right\}, \tag{30a}$$

$$\frac{\partial \eta_j}{\partial t} = -L_{i,j}\left\{ m\frac{\partial f_0}{\partial \eta_j} - \kappa_{i,j}\left[\frac{\partial^2 \eta_j}{\partial r^2} + \left(\frac{1}{R_1}+\frac{1}{R_2}\right)\frac{\partial \eta_j}{\partial r}\right]\right\}, \tag{30b}$$

where it is applied that $\nabla\eta=(\partial\eta/\partial r)\mathbf{r}$, $\nabla^2\eta=\nabla\cdot\nabla\eta=(\partial^2\eta/\partial r^2)+(\nabla\cdot\mathbf{r})(\partial\eta/\partial r)$, and $(\nabla\cdot\mathbf{r})=1/R_1+1/R_2$ with R_1 and R_2 as the principle radii of curvature.

For the considered boundary conditions

$$\eta_i = 1 \quad \text{and} \quad \eta_j = 0 \quad \text{for} \quad r \to 0, \tag{31a}$$

$$\eta_i = 0 \quad \text{and} \quad \eta_j = 1 \quad \text{for} \quad r \to +\infty, \tag{31b}$$

$$\frac{d\eta_i}{dr} = \frac{d\eta_j}{dr} = 0 \quad \text{for} \quad r \to 0, +\infty, \tag{31c}$$

the term $\kappa_{i,j}(1/R_1+1/R_2)\partial\eta_i/\partial r$ forces the grain boundary to move toward its center of curvature.[45] It was however derived[47–49] that for $\ell_{gb} \ll R_1, R_2$, the effect of this extra term on the shape of the phase field profiles is negligible and that conditions (6a) and (6b) are satisfied to leading order with x measured along the normal to the grain boundary. Moreover, if $\ell_{gb} \ll R_1, R_2$, the mean curvatures $1/R_1$ and $1/R_2$ can be considered to be constant within the thin grain boundary region where the phase field variables change their values. Under this assumption, all contours of constant η_i or η_j value move with the same velocity and the grain boundary velocity $v_{i,j}$ is[45]

$$v_{i,j} = \left(\frac{\partial r}{\partial t}\right)_{\eta_i,\eta_j=\text{cte}} = \frac{\left(\frac{\partial \eta_{i/j}}{\partial t}\right)_r}{\left(\frac{\partial \eta_{i/j}}{\partial r}\right)_t}, \tag{32}$$

$$= -L_{i,j}\kappa_{i,j}\left(\frac{1}{R_1}+\frac{1}{R_2}\right), \tag{33}$$

which is normal to the interface and negative when $\mathbf{r}$ is defined to point outward as in Fig. 1(b). In Appendix A, Eqs. (6a), (6b), and (33) are derived in a more general way from an asymptotic analysis.

In the sharp interface limit, the velocity of the grain boundaries in phase field simulations is thus proportional to their local mean curvature. This is in analogy with the sharp interface Gibbs–Thomson law for grain boundary movement,

$$v_{gb} = -\mu_{gb}\sigma_{gb}\left(\frac{1}{R_1}+\frac{1}{R_2}\right), \tag{34}$$

which gives the grain boundary velocity in terms of the grain boundary energy σ_{gb} and mobility μ_{gb}. Relation (34) is expressed in the same coordinate system as Eq. (33). Comparison of both equations yields a relation between the phase field model parameters and the grain boundary energy and mobility,

$$\mu_{gb}\sigma_{gb} = \kappa_{i,j}L_{i,j}. \tag{35}$$

Relations (33) and (35) are valid for symmetrical and asymmetrical interfacial profiles.

To evaluate the validity of approximation (33), the shrinkage rate of a circular grain was determined from phase field

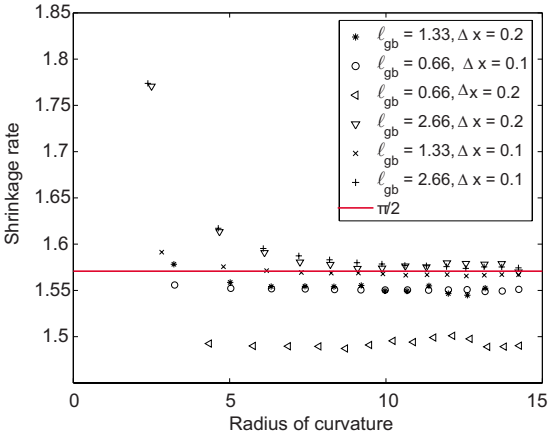

FIG. 10. (Color online) Reduction in grain area per unit of time for a circular grain as a function of the grain radius, obtained from numerical simulations for $\sigma_{gb}=0.25$ and $\mu_{gb}=1$, and different grain boundary widths ℓ_{gb} and grid spacings Δx. For all simulations, $\gamma=1$. The values for κ, m, and L were determined using relations(36a)–(36c) with the appropriate values for $\sigma_{gb}=0.25$, $\mu_{gb}=1$, and ℓ_{gb}. The sharp interface approximation (33) predicts a shrinkage rate equal to $2\pi\mu_{gb}\sigma_{gb}=\pi/2$.

simulations using varying grain boundary widths ℓ_{gb} and grid spacings Δx. A standard finite difference discretization with explicit time stepping was used for the numerical solution. The results are plotted as a function of the grain radius in Fig. 10. The shrinkage rate is constant (which means that the velocity is proportional to the curvature) and the simulation results converge to the sharp interface approximation (33) for $\ell_{gb}/R<1/4$. For the applied discretization technique, a poor resolution results in a too low shrinkage rate: the relative deviations are approximately 0.25%, 1.3%, and 5% for $\ell_{gb}/\Delta x$ equal to 13, 6.6, and 3.3 for $R\gg\ell_{gb}$. These results confirm previous numerical tests.[46]

H. Calculation of the model parameters for uniform systems

From the analysis in the previous subsections, relations can be derived that allow us to calculate appropriate parameters for the phase field equations (1)–(3). The set of model parameters should reproduce a given grain boundary energy σ_{gb} and grain boundary mobility μ_{gb} and result in a diffuse grain boundary width ℓ_{gb} that is prescribed by numerical (accuracy and stability) and computational (computation time and memory) considerations. Combination and rearrangement of Eqs. (12), (28), and (35) gives

$$\kappa=\sigma_{gb}\ell_{gb}\frac{\sqrt{f_{0,\mathrm{interf}}(\gamma)}}{g(\gamma)}\approx\frac{3}{4}\sigma_{gb}\ell_{gb}, \tag{36a}$$

$$L=\frac{\mu_{gb}}{\ell_{gb}}\frac{g(\gamma)}{\sqrt{f_{0,\mathrm{interf}}(\gamma)}}\approx\frac{4}{3}\frac{\mu_{gb}}{\ell_{gb}}, \tag{36b}$$

$$m=\frac{\sigma_{gb}}{\ell_{gb}}\frac{1}{g(\gamma)\sqrt{f_{0,\mathrm{interf}}(\gamma)}}\approx\frac{3}{4}\frac{1}{f_{0,\mathrm{saddle}}(\gamma)}\frac{\sigma_{gb}}{\ell_{gb}}. \tag{36c}$$

The approximated expressions assume that $g(\gamma)\approx 4/3\sqrt{f_{0,\mathrm{interf}}(\gamma)}\approx 4/3\sqrt{f_{0,\mathrm{saddle}}(\gamma)}$, which gives accurate results for γ values around 1.5 (see Fig. 8). If the approximated expressions are not accurate enough, $g(\gamma)$ and $f_{0,\mathrm{interf}}(\gamma)$ can be evaluated from a polynomial fitted through the numerically calculated values of $g(\gamma)$ and $f_{0,\mathrm{interf}}(\gamma)$. Fifth-order polynomials, for example, fit smoothly the calculated data points for $g(\gamma)$ and $f_{0,\mathrm{interf}}(\gamma)$ over a wide range of γ values.

To calculate the model parameters, one must first decide on the value of γ and determine $g(\gamma)$ and $f_{0,\mathrm{interf}}(\gamma)$. With these values, κ, m, and L can be calculated from Eqs. (36a)–(36c). In previous grain growth simulations for uniform systems,[7,12,13,26] γ was always taken equal to 1, giving very satisfactory results. However, the present analysis indicates that $\gamma=1.5$ might be a more appropriate choice, as it results in symmetrical phase field profiles. For symmetrical profiles, the approximations in relations (36a)–(36c) are exact, resulting in simple relations between the model parameters and grain boundary energy and mobility. Moreover, asymmetrical profiles have longer tails for the same grain boundary width (see Fig. 9); the sharp interface approximation (33) may therefore break down at a larger grain size, although this effect is really small.

If the properties of the system are expressed in SI units, namely, σ_{gb} (J/m^2), ℓ_{gb}(m), and μ_{gb} (m^4/J s), the model parameters have the following dimensions, κ (J/m), L (m^3/J s), and m (J/m^3). The parameter γ is dimensionless.

III. SYSTEMS WITH NONUNIFORM GRAIN BOUNDARY PROPERTIES

In this section, the previous analysis is extended to systems with nonuniform grain boundary properties. The purpose is to derive a methodology for calculating appropriate model parameters $\kappa(\theta,\phi)$, $\gamma(\theta,\phi)$, $L(\theta,\phi)$, and m, which reproduce accurately a given grain boundary energy $\sigma_{gb}(\theta,\phi)$ and mobility $\mu_{gb}(\theta,\phi)$ as a function of misorientation θ and grain boundary inclination ϕ. The model formulation and parameters must guarantee a constant diffuse grain boundary width, in order to resolve the movement of all grain boundaries with an equal accuracy in the numerical simulations. If there would be large variations in grain boundary width with misorientation or inclination, the phase field profiles across thinner grain boundary segments would be less resolved than those across wider segments, while the sharp interface approximation breaks down more easily for wider segments. As a consequence, it would be difficult to control the numerical accuracy of the simulations and artificial effects may be introduced.[35]

A. Model formulation for systems with nonuniform grain boundary properties

Anisotropy is introduced in equations (1)–(3) by formulating the parameters κ, γ, and L as a function of the misorientation θ between adjacent grains and the inclination ϕ of the grain boundaries,

$$\frac{\partial\eta_i(\mathbf{r},t)}{\partial t}=-L(\theta,\phi)\frac{\delta F(\eta_1,\eta_2,\ldots,\eta_p)}{\delta\eta_i(\mathbf{r},t)}, \tag{37}$$

with

$$F = \int_V \left[m f_0(\eta_1, \eta_2, \ldots, \eta_p) + \frac{\kappa(\theta,\phi)}{2} \sum_{i=1}^{p} (\nabla \eta_i)^2 \right] dV, \tag{38}$$

and

$$f_0(\eta_1, \eta_2, \ldots, \eta_p) = \sum_{i=1}^{p} \left(\frac{\eta_i^4}{4} - \frac{\eta_i^2}{2} \right) + \sum_{i=1}^{p} \sum_{j>i}^{p} \gamma(\theta,\phi) \eta_i^2 \eta_j^2 + \frac{1}{4}. \tag{39}$$

In the most general case, θ is a vector with three independent coordinates, which define the misorientation between two adjacent grains, and ϕ a is vector with two independent (or three normalized) coordinates, which define the inclination of a grain boundary.[5] An important difference with most phase field models for anisotropic systems is that both the homogeneous free energy and the gradient free energy may be inclination dependent.

The local misorientation and grain boundary inclination can be derived from the local values of the phase field variables and their gradients, resulting in the following model parameter functions:

$$\kappa(\theta,\phi) = \frac{\sum_{i=1}^{p} \sum_{j>i}^{p} \kappa_{i,j}(\phi_{i,j}) \eta_i^2 \eta_j^2}{\sum_{i=1}^{p} \sum_{j>i}^{p} \eta_i^2 \eta_j^2}, \tag{40a}$$

$$\gamma(\theta,\phi) = \frac{\sum_{i=1}^{p} \sum_{j>i}^{p} \gamma_{i,j}(\phi_{i,j}) \eta_i^2 \eta_j^2}{\sum_{i=1}^{p} \sum_{j>i}^{p} \eta_i^2 \eta_j^2}, \tag{40b}$$

and

$$L(\theta,\phi) = \frac{\sum_{i=1}^{p} \sum_{j>i}^{p} L_{i,j}(\phi_{i,j}) \eta_i^2 \eta_j^2}{\sum_{i=1}^{p} \sum_{j>i}^{p} \eta_i^2 \eta_j^2}. \tag{40c}$$

The parameter m is constant throughout the system. Misorientation dependence is thus treated in a discrete way; whereas for each misorientation, the parameters are continuous functions of the grain boundary inclination $\phi_{i,j}$. $\phi_{i,j}$ is a normalized vector that specifies the orientation of the normal to the grain boundary between grains with orientations i and j. We relate the inclination $\phi_{i,j}$ to the local gradients of the phase field variables $\nabla \eta_i$ and $\nabla \eta_j$ using the following function:

$$\phi_{i,j} = \frac{\nabla \eta_i - \nabla \eta_j}{|\nabla \eta_i - \nabla \eta_j|}, \tag{41}$$

in which the two phase field variables are treated in an antisymmetric way, to obtain a vector perpendicular to the grain boundary surface. In the formulation of Kazaryan *et al.*,[50] the local inclination is derived from the gradient of one of the phase field variables, namely, from $\phi_{i,j} = \nabla \eta_i / |\nabla \eta_i|$. However, when the grain boundary energy is inclination dependent, the value at which the order parameter fields cross, varies along the grain boundary and the gradient of each phase field has accordingly a contribution along the tangential to the surface. Since this tangential contribution is equal for both phase field variables, the vector $\nabla \eta_i - \nabla \eta_j$ is always perpendicular to the contour at which the phase field profiles intersect. Formulations (40a)–(40c) allow us to specify for each misorientation individually the value and inclination dependence of the grain boundary energy and mobility. Within a diffuse grain boundary region where η_i and η_j change values, $\kappa(\theta,\phi) = \kappa_{i,j}(\phi_{i,j})$, $\gamma(\theta,\phi) = \gamma_{i,j}(\phi_{i,j})$, and $L(\theta,\phi) = L(\phi_{i,j})$. Near triple junctions, there is a smooth transition between the parameter functions for the misorientations of the intersecting grain boundaries. With formulation (40b), homogeneous free energy (39) reduces to

$$f_0(\eta_1, \eta_2, \ldots, \eta_p) = \sum_{i=1}^{p} \left(\frac{\eta_i^4}{4} + \frac{\eta_i^2}{2} \right) + \sum_{i=1}^{p} \sum_{j>i}^{p} \gamma_{i,j}(\phi_{i,j}) \eta_i^2 \eta_j^2 + \frac{1}{4}. \tag{42}$$

In principle, there are many possibilities to introduce anisotropy in the free-energy functional. An appealing alternative is to assume $\gamma = 1.5$ constant and introduce the anisotropy in the homogeneous free energy through the parameter m and κ, with

$$m(\theta,\phi) = \frac{\sum_{i=1}^{p} \sum_{j>i}^{p} m_{i,j}(\phi_{i,j}) \eta_i^2 \eta_j^2}{\sum_{i=1}^{p} \sum_{j>i}^{p} \eta_i^2 \eta_j^2} \tag{43}$$

and κ as given in Eq. (40a). The advantage is that the phase field profiles are symmetrical for all grain boundaries and that therefore there exist analytical relations between the model parameters and grain boundary energy, mobility, and width. However, application of this model showed that the triple junction angles in the simulations are much more sensitive to modifications of the interfacial width than is the case for formulation (39), although in the sharp interface limit ($\ell_{gb} \gg R_1, R_2$) both models result in correct triple junction angles. Impractical fine grid spacings are consequently required to obtain accurate grain growth simulations. We think that one reason for this difference in behavior in numerical simulations between the two free-energy formulations could be the fact that formulation (39) reduces to Eq. (42), whereas no reduction is possible for formulation (43); as a result, the grain boundary properties are interpolated in a different way in the diffuse regions around the triple junctions.

B. Misorientation dependence

If inclination dependence is neglected, it follows from formulations (40a)–(40c) that $k(\theta) = k_{i,j}$, $\gamma(\theta) = \gamma_{i,j}$ and $L(\theta) = L_{i,j}$ are constant within the diffuse grain boundary region

between grains with orientations i and j. By consequence, relations (36a)–(36c) apply for an individual grain boundary. One difficulty is that now there are different $\gamma_{i,j}$'s for grain boundaries with different energies. These values must be chosen so that each grain boundary has the correct energy, while all grain boundaries have the same width. Due to the complicated relations between the model parameter $\gamma_{i,j}$ and the grain boundary properties, an iterative procedure, described by Algorithm 1, is required to obtain the $\gamma_{i,j}$ for different misorientations.

Algorithm 1 requires, as input, lists of discrete values $\sigma_{\mathrm{gb},k}$ and $\mu_{\mathrm{gb},k}$, the desired grain boundary width ℓ_{gb}, and two initial values γ_{init} and $\sigma_{\mathrm{gb,init}}$. In the first step, the parameter m, which is uniform throughout the system, is calculated using the initial values γ_{init} and $\sigma_{\mathrm{gb,init}}$. In the main step, an iterative procedure is used for each k to calculate κ_k, γ_k, and L_k. To start, a first estimate κ^* and γ^* is made based on a_{init} calculated for γ_{init} or the a_k calculated for the previous misorientation. A new value a_k^* is also computed for κ^* and γ^*. If $a_k^* \neq a_{\mathrm{init}}$, improved values for κ^* and γ^* are calculated based on updated values for a_k^* in subsequent iteration steps until the values for a_k^*, γ^*, and κ^* are self-consistent. Then, the kinetic parameter L_k is calculated using the self-consistent value for a_k. The output of the procedure are the parameter m and a list with the appropriate values for κ_k, γ_k, and L_k.

To be able to calculate $g(\gamma_k)$, $\gamma_k = g^{-1}$, and $f_{0,\mathrm{interf}}(\gamma_k)$ for arbitrary values of γ_k, the numerically calculated function values for $f_{0,\mathrm{interf}}(1/\gamma)$, $g^2(1/\gamma)$, and $(g^2)^{-1}(1/\gamma)$ were interpolated with fifth-order polynomials for γ within the range [0.55 8]. In step 3 of the algorithm, $\gamma^* = g^{-1}$ is calculated via the interpolated function $g^2(1/\gamma)$: $g \rightarrow g^2 \rightarrow 1/\gamma^* \rightarrow \gamma^*$. If all γ_k can be taken close to 1.5, the iterative procedure may be avoided by assuming that $g(\gamma) = (4/3) * \sqrt{f_{0,\mathrm{interf}}} = (4/3) * \sqrt{f_{0,\mathrm{saddle}}}$.

Algorithm 1. Iterative procedure for the calculation of the phase field model parameters for a given set of grain boundary energies $\sigma_{\mathrm{gb},k}$, grain boundary mobilities $\mu_{\mathrm{gb},k}$, and a uniform grain boundary width ℓ_{gb}.[51]

Input:
$\{\sigma_{\mathrm{gb},k}\}$, $\{\mu_{\mathrm{gb},k}\}$, ℓ_{gb}
$\sigma_{\mathrm{gb,init}}$, γ_{init}

Initial Step: Calculate $g(\gamma_{\mathrm{init}})$, $f_{0,\mathrm{interf}}(\gamma_{\mathrm{init}})$, and $a_{\mathrm{init}} = \sqrt{f_{0,\mathrm{interf}}(\gamma_{\mathrm{init}})}/g(\gamma_{\mathrm{init}})$
Calculate m from Eq. (36c) using $\sigma_{\mathrm{gb,init}}$, ℓ_{gb}, $f_{0,\mathrm{interf}}(\gamma_{\mathrm{init}})$, and $g(\gamma_{\mathrm{init}})$

Body:
For each k:
Iterative calculation of κ_k, γ_k, and a_k
1. Calculate $\kappa^* = \sigma_{\mathrm{gb},k}\ell_{\mathrm{gb}}a_{\mathrm{init}}$
2. Calculate $g(\gamma^*) = \sigma_{\mathrm{gb},k}/\sqrt{\kappa^* m}$
3. Calculate $\gamma^* = g^{-1}$
4. Calculate $f_{0,\mathrm{interf}}(\gamma^*)$ and $a_k^* = \sqrt{f_{0,\mathrm{interf}}(\gamma^*)}/g(\gamma^*)$
5. If $a_k^* \neq a_{\mathrm{init}}$, $a_{\mathrm{init}} = a_k^*$ and go to 1,
else $\kappa_k = \kappa^*$, $\gamma_k = \gamma^*$, $a_k = a^*$
Calculate L_k from Eq. (36b) using $\mu_{\mathrm{gb},k}$, ℓ_{gb}, and a_k

Output:
m, $\{\kappa_k\}$, $\{\gamma_k\}$, $\{L_k\}$

At the beginning of the procedure, it is arbitrarily chosen that $\gamma(\theta_{\mathrm{init}}) = \gamma_{\mathrm{init}}$. The parameter values for the other misorientations follow from this choice. For different initial values, a different set of model parameters is obtained, which results in the same grain boundary energies, mobilities, and uniform grain boundary width. We advice to choose γ_{init} around 1.5 for a θ_{init} within the range of the θ_k values, in order to obtain close to symmetrical grain boundary profiles.

As the function $g(\gamma)$ flattens for larger values of γ, there is a limit on the ratio $\sigma_{\max}/\sigma_{\min}$ that can be covered by the model. From the numerically calculated data for $g(\gamma_{i,j})$, it is derived that for γ in the range [0.9 2.65], $g(\gamma_{i,j}) \in [0.36\ 0.56]$ and $\sigma_{\max}/\sigma_{\min} = g_{\max}^2/g_{\min}^2 = 2.38$; for $\gamma \in [0.75\ 3.45]$, $g(\gamma_{i,j}) \in [0.30\ 0.59]$ and $\sigma_{\max}/\sigma_{\min} = g_{\max}^2/g_{\min}^2 = 3.73$; for $\gamma \in [0.53\ 6.5]$, $g(\gamma_{i,j}) \in [0.12\ 0.65]$ and $\sigma_{\max}/\sigma_{\min} = g_{\max}^2/g_{\min}^2 = 29.4$; for $\gamma \in [0.52\ 8]$, $g(\gamma_{i,j}) \in [0.0985\ 0.67]$ and $\sigma_{\max}/\sigma_{\min} = g_{\max}^2/g_{\min}^2 = 45.8$; and for $\gamma \in [0.52\ 40]$, $g(\gamma_{i,j}) \in [0.0985\ 0.76]$ and $\sigma_{\max}/\sigma_{\min} = g_{\max}^2/g_{\min}^2 = 60.4$. The latter may be considered as the practical limit.

C. Inclination dependence

For a given inclination $\phi_{i,j}$, the parameters $\kappa_{i,j}(\phi_{i,j})$, $\gamma_{i,j}(\phi_{i,j})$, $L_{i,j}(\phi_{i,j})$, and m are constant along the normal to the grain boundary. In Appendix A, it is explained how to extend the asymptotic analysis described in Refs. 47–49 to equations (37)–(39). It is derived that the profiles of the phase field variables across a grain boundary satisfy Eqs. (6a) and

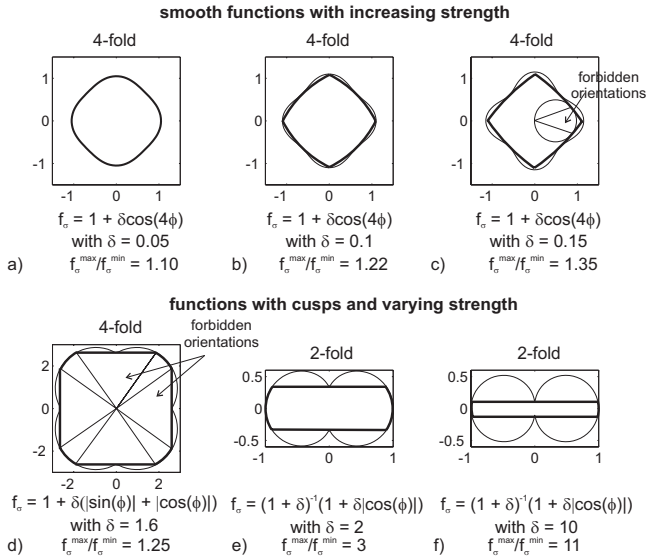

FIG. 11. Polar plots of a number of inclination-dependent functions $f_\sigma(\phi)$ for 2D systems. The equilibrium shape of the crystal, determined according to Wulff's theorem (Ref. 54) is plotted in bold. It contains only those orientations for which $f_\sigma(\phi)+df_\sigma(\phi)/d\phi>0$. For simulations, the nonconvex parts must be regularized as described in Refs. 55–57.

(6b) to leading order for $\ell_{\mathrm{gb}} \ll R_1, R_2$, with x measured along the normal to the surface and $\kappa_{i,j}=\kappa_{i,j}(\phi_{i,j})$ and $\gamma_{i,j}=\gamma_{i,j}(\phi_{i,j})$ constant along the profiles. Consequently, relations (12) and (28), with $g(\gamma_{i,j})$ and $f_{0,\mathrm{interf}}(\gamma_{i,j})$ as calculated for uniform systems, apply along each direction $\phi_{i,j}$, giving

$$\sigma_{\mathrm{gb}}(\theta_{i,j},\phi)=g(\gamma_{i,j}(\phi_{i,j}))\sqrt{\kappa_{i,j}(\phi_{i,j})m}, \tag{44}$$

and

$$\ell_{\mathrm{gb}}=\sqrt{\frac{\kappa_{i,j}(\phi_{i,j})}{mf_{0,\mathrm{interf}}(\gamma_{i,j}(\phi_{i,j}))}}, \tag{45}$$

in which $\sigma_{\mathrm{gb}}(\theta_{i,j},\phi)$ refers to the inclination-dependent specific energy of a grain boundary between the grains with orientations i and j. Furthermore, it is obtained that in the sharp interface limit, the normal velocity of each point on a grain boundary equals

$$\begin{aligned} v_{\mathrm{gb},n}=&-L_{i,j}(\phi_{i,j})\frac{\sqrt{\kappa_{i,j}(\phi_{i,j})}}{g(\gamma_{i,j}(\phi_{i,j}))}\left\{\frac{1}{R_1}\left[\sqrt{\kappa_{i,j}(\phi_{i,j})}g(\gamma_{i,j}(\phi_{i,j}))\right.\right.\\ &\left.+\frac{\partial^2(\sqrt{\kappa_{i,j}(\phi_{i,j})}g(\gamma_{i,j}(\phi_{i,j})))}{\partial\alpha_1^2}\right]\\ &+\frac{1}{R_2}\left[\sqrt{\kappa_{i,j}(\phi_{i,j})}g(\gamma_{i,j}(\phi_{i,j}))\right.\\ &\left.\left.+\frac{\partial^2(\sqrt{\kappa_{i,j}(\phi_{i,j})}g(\gamma_{i,j}(\phi_{i,j})))}{\partial\alpha_2^2}\right]\right\}, \end{aligned} \tag{46}$$

with $\phi_{i,j}$ [defined as in Eq. (41)] as the normal direction and R_1, R_2, α_1, and α_2 defined in a curvilinear coordinate system as shown in Fig. 1(b). For sharp interface systems with inclination dependence, Herring's formula[52,53] prescribes a normal velocity $v_{\mathrm{gb},n}$,

$$\begin{aligned} v_{\mathrm{gb},n}=&-\mu_{\mathrm{gb}}(\phi)\left\{\frac{1}{R_1}\left[\sigma_{\mathrm{gb}}(\phi)+\frac{\partial^2\sigma_{\mathrm{gb}}(\phi)}{\partial\alpha_1^2}\right]\right.\\ &\left.+\frac{1}{R_2}\left[\sigma_{\mathrm{gb}}(\phi)+\frac{\partial^2\sigma_{\mathrm{gb}}(\phi)}{\partial\alpha_2^2}\right]\right\}, \end{aligned} \tag{47}$$

with $\sigma_{\mathrm{gb}}(\phi)+\frac{\partial^2\sigma_{\mathrm{gb}}(\phi)}{\partial\alpha_1^2}$ and $\sigma_{\mathrm{gb}}(\phi)+\frac{\partial^2\sigma_{\mathrm{gb}}(\phi)}{\partial\alpha_2^2}$ as the diagonal elements of the grain boundary stiffness tensor. Comparison of Eq. (46) with Eq. (47), considering relation (44), shows that relation (35) as well remains valid for individual directions $\phi_{i,j}$, giving

$$\mu_{\mathrm{gb}}(\theta_{i,j},\phi)\sigma_{\mathrm{gb}}(\theta_{i,j},\phi)=\kappa_{i,j}(\phi_{i,j})L_{i,j}(\phi_{i,j}), \tag{48}$$

with $\sigma_{\mathrm{gb}}(\theta_{i,j},\phi)$ and $\mu_{\mathrm{gb}}(\theta_{i,j},\phi)$ defined as in relation (44).

To formulate the inclination-dependent model parameters $\kappa_{i,j}(\phi_{i,j})$, $\gamma_{i,j}(\phi_{i,j})$, and $L_{i,j}(\phi_{i,j})$, it is assumed that the grain boundary properties of the system are characterized by a set of inclination-dependent grain boundary energies $\sigma_{\mathrm{gb},k}(\phi)=\bar{\sigma}_{\mathrm{gb},k}f_{\sigma,k}(\phi)$ and mobilities $\mu_{\mathrm{gb},k}(\phi)=\bar{\mu}_{\mathrm{gb},k}f_{\mu,k}(\phi)$, where k refers to different misorientations (the difference in orientation between grains with orientations i and j, for different combinations of i and j) and ϕ is the inclination of the boundary measured with respect to the crystal lattice of one of the adjacent grains. The grain boundary energies and mobilities may have different inclination dependences and the inclination dependence may vary with misorientation. Comparison of Eq. (46) with Eq. (47) indicates that the choice of appropriate inclination-dependent functions for the model parameters is considerably simplified if $\kappa_{i,j}(\phi_{i,j})$ and $g^2(\gamma_{i,j})$ are assumed to have the same inclination-dependent factor as the specific grain boundary energy, namely, $\kappa_k(\phi)=\bar{\kappa}_k f_{\sigma,k}(\phi)$ and $g^2(\gamma_k(\phi))=g^2(\bar{\gamma}_k)f_{\sigma,k}(\phi)$. Equation (46) then simplifies to

$$\begin{aligned} v_{\mathrm{gb},n}=&-L_{i,j}(\phi_{i,j})\left[\frac{1}{R_1}\left(\kappa_{i,j}(\phi_{i,j})+\frac{\partial^2\kappa_{i,j}(\phi_{i,j})}{\partial\alpha_1^2}\right)\right.\\ &\left.+\frac{1}{R_2}\left(\kappa_{i,j}(\phi_{i,j})+\frac{\partial^2\kappa_{i,j}(\phi_{i,j})}{\partial\alpha_2^2}\right)\right], \end{aligned} \tag{49}$$

and it follows from relation (48) that $L_k(\phi)$ has the same inclination-dependent factor as the grain boundary mobility $\mu_{\mathrm{gb}}(\phi)$. Unfortunately, this choice of the model parameter functions does not guarantee a constant grain boundary width for large variations in grain boundary energy [see Eq. (45) and Fig. 8]. Therefore, two different approaches are proposed for the two extreme cases of weak (smooth boundaries) and strong (faceted boundaries) inclination dependence of the grain boundary energy. To support the explanation, a number of inclination-dependent factors $f_\sigma(\phi)$ with different shapes and strengths, typically used for two-dimensional (2D) systems, are shown in Fig. 11. More functions, also for three-dimensional (3D) systems, are available in the literature.[58,59] Intermediate cases, as for example plots (c) and (e) in Fig. 11, can be treated by both approaches. Since grain growth may be considered as a slow process and attachment kinetics in metals are relatively fast, it is assumed

in the further explanation that the shape of the crystals is primarily determined by the inclination dependence of the grain boundary energy.

1. Weak inclination dependence

When the inclination dependence of the specific grain boundary energy is smooth, all or most grain boundary inclinations may occur from a thermodynamic point of view. It is thus important that the set of model parameters reflects the full inclination dependence of the specific grain boundary energy, stiffness, and mobility to obtain correct grain boundary behavior in the simulations. On the other hand, the variations in grain boundary energy are small. Therefore, the following inclination-dependent parameter functions are most convenient:

$$\kappa_{i,j}(\phi_{i,j}) = \bar{\kappa}_k f_{\sigma,k}(\phi), \tag{50a}$$

$$\gamma_{i,j}(\phi_{i,j}) = g^{-1} \text{with}$$
$$g^2(\gamma_{i,j}) = g^2(\bar{\gamma}_k) f_{\sigma,k}(\phi), \tag{50b}$$

and

$$L_{i,j}(\phi_{i,j}) = \bar{L}_k f_{\mu,k}(\phi), \tag{50c}$$

where k is the misorientation between grains i and j, ϕ is the inclination of the boundary defined with respect to the crystal lattice of 1 of the adjacent grains and $\phi_{i,j}$ the inclination angle defined with respect to the system [by Eq. (41)] and related to $\phi_{i,j}$ through the orientations i and j. The values for m, $\bar{\gamma}_k$=, $g^2(\bar{\gamma}_k)$, $\bar{\kappa}_k$, and $\bar{L}_k$ can be calculated for each misorientation θ_k with Algorithm 1, using the given $\bar{\sigma}_{\text{gb},k}$, $\bar{\mu}_{\text{gb},k}$ and an appropriate value for ℓ_{gb} as input data. It can be verified for parameter functions (50a)–(50c) that variations in grain boundary width with inclination are negligible for weak and moderate inclination dependence of the specific grain boundary energy, since the γ dependence of the ratio $a_k = g(\gamma_k)/\sqrt{f_{0,\max}(\gamma_k)}$ may be considered to be constant within limited ranges of γ_k values. For γ_k varying between 0.9 and 2.65, the deviations in grain boundary width are smaller than 0.81%; for γ_k between 0.75 and 3.45, they are below 1.6%.

For γ_k not too far from 1.5, $g(\gamma_k)$ is approximated closely by the analytical function for $4/3\sqrt{f_{0,\text{saddle}}(\gamma_k)}$ (see Fig. 8). Then, a differentiable function for $\gamma_k(\phi_k)$,

$$\gamma_k(\phi_k) = \frac{-\frac{9}{4}g^2(\bar{\gamma}) f_{\sigma,k}(\phi_k) - 1}{\frac{9}{2}g^2(\bar{\gamma}) f_{\sigma,k}(\phi_k) - 2}, \tag{51}$$

can be obtained from relation (15). More generally, differentiable functions for the inclination dependence of $\gamma_k(\phi_k)$ can be obtained by fitting polynomials through the numerically calculated data points for $g(\gamma_k)$ within the ranges of $g(\gamma_k)$ values of interest, namely, those covering $f_\sigma^{\min}$ and $f_\sigma^{\max}$, although for large ratios $f_\sigma^{\max}/f_\sigma^{\min}$, the procedure for strong inclination dependence is more appropriate.

In most phase field models, the inclination dependence of the grain boundary energy is completely treated in the gradient term of the free-energy functional, resulting in straightforward inclination-dependent relations between the model parameters and the grain boundary energy. However, in this way the variations in grain boundary width with inclination are linearly proportional to the variations in grain boundary energy. Moreover, in these models the inclination dependence of the gradient term contributes to the inclination dependence of the grain boundary mobility. In relation (50a)–(50c), by contrast, the inclination dependence of the kinetic coefficient is directly related to that of the grain boundary mobility.

2. Strong inclination dependence

In the case of strong anisotropy, there are large variations in specific grain boundary energy with inclination. The inclination-dependent parameter functions (50a)–(50c) may then result in variations in grain boundary width with inclination and more complicated functions would be required to interpolate $\gamma = g^{-1}$ over a wider range of γ_k values in Eqs. (50b). Moreover, due to strong variations in σ_{gb} with inclination, only a limited number of discrete inclinations, or very narrow inclination ranges, are thermodynamically stable, namely, those for which $f_\sigma(\phi) + df_\sigma(\phi)/d\phi > 0$ (or the trace of the stiffness tensor is positive for 3D systems). The plots (d)–(f) in Fig. 11 also show that the crystal shape is mainly determined by the extrema of the inclination-dependent factor $f_\sigma(\phi)$ and that within a range of stable inclinations, the variation of $f_\sigma(\phi)$ is very limited. It is actually most important that the parameters in the phase field model reproduce accurately the extrema of the inclination-dependent factor. In the case of strong inclination dependence, the following procedure is accordingly more appropriate to determine inclination-dependent functions for the model parameters in the phase field model.

First, a set of discrete values $\kappa_{k,l}$, $\gamma_{k,l}$, $L_{k,l}$, and m is calculated using Algorithm 1 with a list of $\sigma_{\text{gb}}(\theta_k, \phi_{k,l})$ and $\mu_{\text{gb}}(\theta_k, \phi_{k,l})$ values and an appropriate grain boundary width ℓ_{gb} as input. The $\phi_{k,l}$ are discrete inclinations for which $f_{\sigma,k}(\phi)$ is extremal. The iterative calculation in the body of Algorithm 1 is now performed for each extremal inclination $\phi_{k,l}$ for each misorientation θ_k. The inclination-dependent model parameters for each misorientation k are subsequently formulated as

$$\kappa_{i,j}(\phi_{i,j}) = \bar{\kappa}_k f'_{\sigma,k}(\phi), \tag{52a}$$

$$\gamma_{i,j}(\phi_{i,j}) = \bar{\gamma}_k f''_{\sigma,k}(\phi), \tag{52b}$$

$$L_{i,j}(\phi_{i,j}) = \bar{L}_k f_{\mu,k}(\phi). \tag{52c}$$

The functions $f'_{\sigma,k}(\phi)$ and $f''_{\sigma,k}(\phi)$ have cusps and extrema at the same inclinations as $f_{\sigma,k}(\phi)$, the inclination-dependent factor of the specific grain boundary energy. Furthermore, the values of $\bar{\kappa}_k$ and $\bar{\gamma}_k$ are taken so that the extremal values of $\bar{\kappa}_k f'_{\sigma,k}(\phi)$ and $\bar{\gamma}_k f'_{\sigma,k}(\phi)$ equal the $\kappa_{k,l}$ and $\gamma_{k,l}$ calculated in the first step for the extremal values of the specific grain boundary energies. An easy way to fulfill these requirements is to give $f'_{\sigma,k}$ and $f''_{\sigma,k}$ a similar form as $f_{\sigma,k}$, with, for example, for the function plotted in Fig. 11(d),

$$\delta'_k = \frac{\kappa_{\max}/\kappa_{\min} - 1}{\sqrt{2} - \kappa_{\max}/\kappa_{\min}},$$

TABLE I. (Color online) Triple junction angles as obtained in simulations for a triple junction in equilibrium (Y) and one in steady-state movement (T). The effect of grain boundary width ℓ_{gb} and grid spacing Δx was studied for three different configurations, with a theoretically expected value for the angle β_c equal to 102, 6°;120°; and 138, 15°.

Geometries	Equilibrium (Y) 		Steady State (T) 
Young's law	β_c=102, 60°	β_c=120, 00°	β_c=138, 15°
	[$\cos(\beta_c/2)$=0.625]	[$\cos(\beta_c/2)$=0.500]	[$\cos(\beta_c/2)$=0.357]
Δx=0.2, ℓ_{gb}=0.5	110,0 (Y)	121,3 (Y)	140,2 (Y)
	[0.568]	[0.490]	[0.343]
	107,5 (T)	119,8 (T)	139,9 (T)
	[0.594]	[0.502]	[0.343]
Δx=0.2, ℓ_{gb}=1	109.1 (Y)	120,3 (Y)	139,2 (Y)
	[0.577]	[0.498]	[0.356]
	103,8 (T)	117,3 (T)	138,3 (T)
	[0.617]	[0.520]	[0.356]
Δx=0.1, ℓ_{gb}=0.5	109,1 (Y)	120,3 (Y)	139,2 (Y)
	[0.577]	[0.498]	[0.353]
	105,7 (T)	118,4 (T)	138,7 (T)
	[0.606]	[0.512]	[0.353]
Δx=0.1, ℓ_{gb}=1	108,8 (Y)	120,3 (Y)	139,0 (Y)
	[0.582]	[0.498]	[0.357]
	104,7 (T)	117.6 (T)	138,2 (T)
	[0.619]	[0.516]	[0.357]
Δx=0.1,ℓ_{gb}=2	108,8 (Y)	120,3 (Y)	139,2 (Y)
	[0.592]	[0.498]	[0.369]
	103,3 (T)	116.6 (T)	136,7 (T)
	[0.617]	[0.523]	[0.369]

$$\bar{\kappa}_k = \frac{\kappa_{\max}}{1+\sqrt{2}\delta'_k} = \frac{\kappa_{\min}}{1+\delta'_k},$$

or for the functions plotted in Figs. 11(e) and 11(f),

$$\delta'_k = \kappa_{\max}/\kappa_{\min} - 1,$$

$$\bar{\kappa}_k = \kappa_{\max} = \kappa_{\min}(1+\delta'_k).$$

In both cases $\kappa_{\max}$ and $\kappa_{\min}$ are the $\kappa_{k,l}$ calculated for the inclination l for which the specific grain boundary energy is maximal or minimal. As the range of stable inclinations and the variation of the specific grain boundary energy within these ranges are extremely small and primarily determined by the extrema, the inclination dependence of the homogeneous free energy is formulated directly for the parameter γ.

D. Force balance at edges and multijunctions

If the specific grain boundary energy of each grain boundary is correctly reproduced in the simulations, one may expect that Young's law, and more generally the Herring relation, are fulfilled at the triple junctions since they follow from energy considerations.[53,60] For a number of phase field models it has been verified that in the limit of sharp interfaces ($\ell_{gb} \ll R_1, R_2$), surface tensions are balanced at edges and triple junctions.[48,61] In Appendix A, a similar analysis is applied to the present model. One result is that the force due to its specific energy of a grain boundary between grains i and j acting on a plane that cuts the boundary perpendicularly equals to leading order

$$f = \frac{\partial}{\partial \alpha_1}\left\{\kappa_{i,j}\int_0^\infty \left[\left(\frac{\partial \eta_i}{\partial r}\right)^2 + \left(\frac{\partial \eta_j}{\partial r}\right)^2\right]dr\right\}\mathbf{r} - \kappa_{i,j}\left\{\int_0^\infty \left[\left(\frac{\partial \eta_i}{\partial r}\right)^2 + \left(\frac{\partial \eta_j}{\partial r}\right)^2\right]dr\right\}\mathbf{t}_1 = \frac{\partial \sigma_{gb}}{\partial \alpha_1}\mathbf{r} - \sigma_{gb}\mathbf{t}_1, \quad (53)$$

with $\mathbf{r}$, $\mathbf{t}_1$, and $\mathbf{t}_2$ curvilinear; $\mathbf{t}_1$ perpendicular to the plane; and $\mathbf{t}_2$ common to the plane and the grain boundary surface. The tangential term drives the grain boundary to move toward its center of curvature to shorten its length. The radial term is a torque that forces the grain boundary to reorient

itself toward an orientation with lower energy.

Considering a closed surface that cuts all grain boundaries meeting at an edge or multijunction perpendicularly, application of Neother's theorem subsequently gives

$$\sum_k \frac{\partial \sigma_{\mathrm{gb}}(\theta_k, \alpha_{1,k})}{\partial \alpha_{1,k}} \mathbf{r}_k - \sigma_{\mathrm{gb}}(\theta_k, \alpha_{1,k}) \mathbf{t}_{1,k} = 0, \tag{54}$$

where the sum is taken over all grain boundary segments that meet at the junction. r_k and $t_{1,k}$ are the radial and tangential curvilinear coordinate for grain boundary k, $\alpha_{1,k}$ is the inclination angle measured in the plane ($\mathbf{r}_k$, $\mathbf{t}_{1,k}$), and the intersection line of the grain boundaries is directed along $\mathbf{t}_{2,1} = \mathbf{t}_{2,2} = \mathbf{t}_{2,k}$. Equation (54) gives exactly the same force balance requirements for edges and multijunctions as obtained in sharp interface models.[60]

The effect of the diffuse grain boundary width ℓ_{gb} and the grid spacing Δx on the triple junction angles obtained in numerical simulations was studied for junctions in equilibrium (Y) and in steady-state motion (T) (see Table I). The triple junction angle β_c in the simulations was calculated from the curvature of the curved boundaries for the T geometry and from the slope of the diagonal lines for the Y geometry. Both measures were determined from the contours at the middle of the interface where two phase fields cross. In Table I, the angles obtained in the simulations are compared with the theoretically expected value for three different combinations of grain boundary energies. The cosine of the angles is also listed, as it is in fact this quantity that determines the curvature and the movement of the intersecting grain boundaries. For $\beta_c \geq 120°$, the theoretical values are very well reproduced for $\ell_{\mathrm{gb}}/\Delta x > 5$, which is not more restrictive as the requirement for accurate curvature driven grain boundary movement (see Sec. II G). Those obtained during steady-state motion are slightly smaller than the equilibrium angles. Since this deviation increases with grain boundary width, we devote it to the diffuse character of the boundaries. Probably, at and near the triple junction, the two curved boundaries attract each other from the outside. For $\beta_c < 120°$, the angle β_c itself is less well reproduced. However, for small angles, the cosine varies less with its argument. Therefore, $\cos(\beta_c)$, and consequently the grain boundary curvature and velocity, are reproduced with an equal accuracy as is the case for $\beta_c \geq 120°$, in the simulations for steady-state motion (T). For the junctions in equilibrium (Y), it was difficult to measure accurately the small triple junction angles ($\beta_c < 120°$); the angle had to be determined from a few grid points since the diagonal lines have the tendency to meet the system boundaries perpendicularly, affecting the inclination of the line up to close to the triple junction for small angles. Although the results obtained for the configuration for steady-state motion show that a triple junction angle of $\beta_c = 102,6°$ is also well reproduced in the simulations. For larger differences between $\sigma_{\mathrm{gb,max}}$ and $\sigma_{\mathrm{gb,min}}$, i.e., for triple junction angles smaller than 102.6° or larger than 138.15°, an increasing ratio $\ell_{\mathrm{gb}}/(\Delta x)$ is required to obtain the same accuracy, also for the steady-state geometry.

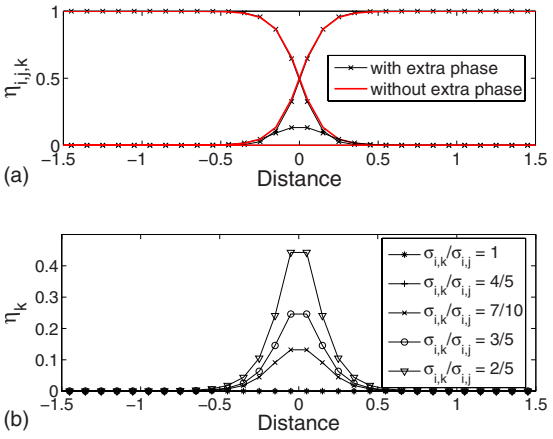

FIG. 12. (Color online) Simulation results that are obtained when the η dependence of the parameter κ is considered in the driving force: (a) effect of an extra phase field variable, $\eta_k \neq 0$, on the profiles of the phase field variables η_i and η_j for $\sigma_{i,k}/\sigma_{i,j} = 7/10$, and (b) profiles of the extra phase field variable η_k for different ratios of $\sigma_{i,k}/\sigma_{i,j}$.

E. Difficulties of a fully variational approach with respect to misorientation dependence

Since κ is a function of the phase field variables and their gradients, in a fully variational approach, the contribution from the gradient energy in the thermodynamic driving forces[62] $\partial F/\partial \eta_i$ should be calculated as[41]

$$\frac{\delta}{\delta \eta_i} \int_V \left[\frac{\kappa}{2} \sum_{j=1}^{p} (\nabla \eta_j)^2 \right] dV = \frac{1}{2} \left(\frac{\partial \kappa}{\partial \eta_i} \right) \sum_{j=1}^{p} (\nabla \eta_j)^2 - \nabla \cdot \left[\frac{1}{2} \left(\frac{\partial \kappa}{\partial \nabla \eta_i} \right) \sum_{j=1}^{p} (\nabla \eta_j)^2 + \kappa \nabla \eta_i \right], \tag{55a}$$

with

$$-\nabla \cdot \left[\frac{1}{2} \left(\frac{\partial \kappa}{\partial \nabla \eta_i} \right) \sum_{j=1}^{p} (\nabla \eta_j)^2 \right] = -\frac{1}{2} \sum_{j=1}^{p} (\nabla \eta_j)^2 \nabla \cdot \left[\frac{\partial \kappa}{\partial \nabla \eta_i} \right] - \frac{1}{2} \frac{\partial \kappa}{\partial \nabla \eta_i} \cdot \nabla \left[\sum_{j=1}^{p} (\nabla \eta_j)^2 \right], \tag{55b}$$

$$-\nabla \cdot \frac{\partial \kappa}{\partial \nabla \eta_i} = -\nabla \cdot \sum_{j \neq i}^{p} \left[\frac{\partial \kappa}{\partial \phi_{i,j}} \frac{\partial \phi_{i,j}}{\partial \nabla \eta_i} \right] = -\sum_{j \neq i}^{p} \left[\left(\frac{\partial^2 \kappa}{\partial \phi_{i,j}^2} \nabla \phi_{i,j} + \sum_{k=1}^{p} \frac{\partial^2 \kappa}{\partial \eta_k \partial \phi_{i,j}} \nabla \eta_k \right) \cdot \frac{\partial \phi_{i,j}}{\partial \nabla \eta_i} \right]$$

$$-\sum_{j\neq i}^{p}\frac{\partial\kappa}{\partial\phi_{i,j}}\nabla\cdot\left[\frac{\partial\phi_{i,j}}{\partial\nabla\eta_i}\right], \tag{55c}$$

and

$$-\nabla\cdot[\kappa\nabla\eta_i]=-(\nabla\kappa)\cdot(\nabla\eta_i)-\kappa\nabla^2\eta_i=-\sum_{j=1}^{p}\left(\frac{\partial\kappa}{\partial\eta_j}\right)\times(\nabla\eta_j)\cdot(\nabla\eta_i)-\sum_{j=1}^{p}\sum_{k\neq j}^{p}\left(\frac{\partial\kappa}{\partial\phi_{j,k}}\right)\times(\nabla\phi_{j,k})\cdot(\nabla\eta_i)-\kappa\nabla^2\eta_i. \tag{55d}$$

The derivatives of $\kappa_{i,j}$ with respect to the gradients of the phase field variables, $\partial\kappa_{i,j}/\partial\nabla\eta_i$, give rise to a driving force that rotates the grain boundary toward a direction with lower energy, which is observed on a mesoscale for metals. The derivatives of κ with respect to the phase field variables, $\partial\kappa/\partial\eta_i$, result in a driving force that changes the local misorientation toward one with a lower energy, by changing the local values of the phase field variables. For instance, if $\kappa_{i,k}=\kappa_{j,k}<\kappa_{i,j}$, the value of κ in the diffuse grain boundary region between grains i and j is lowered when the phase field variable $\eta_k(x)$ takes a finite value at the interface since Eq. (40a) then gives

$$\kappa=\frac{\kappa_{i,j}\eta_i^2\eta_j^2+\kappa_{i,k}\eta_i^2\eta_k^2+\kappa_{j,k}\eta_j^2\eta_k^2}{\eta_i^2\eta_j^2+\eta_i^2\eta_k^2+\eta_j^2\eta_k^2}<\frac{\kappa_{i,j}\eta_i^2\eta_j^2}{\eta_i^2\eta_j^2}=\kappa_{i,j}.$$

Finite values for η_k at the grain boundary between grains i and j give also rise to extra positive contributions in the free energy, namely, $(\kappa/2)(\nabla\eta_k)^2$, $\gamma_{i,k}\eta_i^2\eta_k^2$, and $\gamma_{j,k}\eta_j^2\eta_k^2$. However, for a large enough difference between $\kappa_{i,k}$ and $\kappa_{i,j}$, the decrease in the free energy due to the local reduction in the value of κ overcomes the increase due to the extra terms in the free energy. This is illustrated in Fig. 12. The presence of an extra phase field variable in the diffuse grain boundary region disturbs the original profiles for $\eta_i(x)$ and $\eta_j(x)$. The magnitude of the contribution from the third phase field variable η_k depends on the relative values of the grain boundary energies $\sigma_{i,j}$, $\sigma_{i,k}$, and $\sigma_{j,k}$. As a result, the specific grain boundary energy and the grain boundary velocity in the simulations is lower than expected from relations (44) and (46), and the equilibrium angles between intersecting grain boundaries at triple junctions deviate from the theoretical. If more phase field variables are added to the representation, several extra contributions may appear at a grain boundary. Remark that expression (42) for the homogeneous free energy does not give rise to such a driving force for relaxation with respect to misorientation.

This local relaxation with respect to misorientation at grain boundaries is indeed relevant for diffuse boundaries. However, in the case of metals, the diffuse character of the grain boundaries is artificially introduced in phase field models to avoid tracking of the moving grain boundaries. In reality, grain boundaries in metals are atomically sharp transitions from one crystal orientation to another. Local relaxations at grain boundaries are on the atomistic scale and should not be treated explicitly in mesoscale grain growth simulations. In fact, their effect is already accounted for in the mesoscopic values of the specific grain boundary energy and mobility. To obtain in the phase field simulations the grain boundary behavior observed for metals and to reproduce the parameter relations (36a)–(36c) exactly for individual grain boundaries and inclinations, the local values of κ, γ, and L must be considered as fixed for a given grain configuration. The η dependence of κ is by consequence merely to locate and characterize the grain boundaries and must be omitted in the derivation of the driving force, giving

$$(1/2)(\partial\kappa/\partial\eta_i)\sum_{j=1}^{p}(\nabla\eta_j)^2=0, \tag{56a}$$

$$\sum_{k=1}^{p}\frac{\partial^2\kappa}{\partial\eta_k\partial\phi_{i,j}}\nabla\eta_k=0, \tag{56b}$$

and

$$\sum_{j=1}^{p}\frac{\partial\kappa}{\partial\eta_j}(\nabla\eta_j)\cdot(\nabla\eta_i)=0 \tag{56c}$$

in Eqs. (55a), (55c), and (55d). Note that terms (56a)–(56c) equal zero anyway within grains {where $\Sigma_i\Sigma_{j>i}\eta_i^2\eta_j^2=0$ and $\Sigma[\nabla(\eta_i)^2=0]$} and at grain boundaries [where $\kappa=\kappa_{i,j}(\phi_{i,j})$ does not directly depend on the phase field variables η_i]. By consequence, all results from the sharp interface asymptotic derivation in Appendix A remain valid if restrictions (56a)–(56c) are applied. Only at junctions where three or more grain boundaries intersect, a finite contribution is neglected by omitting the η dependence of κ. The results in Table I and other applications of the model[37,63] show that the theoretical equilibrium angles at triple junctions are well reproduced, if the resolution of the numerical technique is high enough. Nevertheless, it remains to be analyzed in more detail if and to which extent restrictions (56a)–(56c) affect, for example, the kinetic behavior of multijunctions in the simulations.

To allow a fully variational derivation of the kinetic equations, the free-energy functional should be formulated in such a way that the presence of extra phase field variables at interfaces give rise to an increase in the grain boundary energy for any ratio of the parameters. This is the case for equations (1) and (2) with constant model parameters. For the model for nonuniform grain boundary properties, the contribution from extra phase field variables at grain boundaries is largely reduced when using higher powers of the phase field variables in Eqs. (40a)–(40c), namely,

$$\kappa=\frac{\kappa_{i,j}\eta_i^{2a}\eta_j^{2a}}{\eta_i^{2a}\eta_j^{2a}},$$

with $a>1$. However, ever increasing powers are required for larger ratios of $\sigma_{\max}/\sigma_{\min}$, which is impractical for the numerical solution. Other approaches have been proposed to avoid or limit the presence of extra phase field variables at interfaces.[33,64,65] Still, it seems to be extremely difficult to formulate a free energy for diffuse interface systems that avoids completely the presence of extra phases at grain boundaries for arbitrary systems (arbitrary number of orien-

tations, arbitrarily high ratio of $\sigma_{gb,max}/\sigma_{gb,min}$) and is also applicable for numerical simulations. Moreover, in other mesoscale simulation techniques for grain growth, such as the Monte Carlo technique,[16] the local grain boundary energy is also determined based on the orientations of the neighboring grid points and changes *ad hoc* when the orientation of one of the neighboring grid points has changed due to grain boundary movement. Local changes in the misorientation, driven by the possibility to obtain a lower value for the specific grain boundary energy, are not considered either.

IV. CONCLUSIONS

A generalized phase field model has been formulated to perform simulations for grain growth in anisotropic systems with a high controllability of the numerical accuracy. Furthermore, an iterative algorithm is derived to calculate an appropriate set of misorientation-dependent model parameters that reproduces the given grain boundary energy and mobility. Inclination and misorientation dependence of the grain boundary energy is reflected by both the homogeneous and gradient contributions in the free energy. The proposed model formulation and model parameter choice guarantee a constant diffuse grain boundary width in order to resolve the movement of all grain boundaries with the same accuracy. The model can describe arbitrary misorientation and inclination dependence of the grain boundary energy and mobility, such as low-energy cusps in the grain boundary energy for high-angle misorientations and arbitrarily strong inclination dependence of the grain boundary properties.

The free energy and the diffuse profiles of the phase field variables at grain boundaries have been analyzed using a combined analytical and numerical approach. Properties related to the specific grain boundary energy and diffuse interface width were calculated numerically for a large range of values of the dimensionless model parameter γ. The calculated data were interpolated using polynomials and other analytical functions. In this way, relationships with very high accuracy are obtained between the model parameters and grain boundary properties. The width of the diffuse grain boundaries in the phase field description is defined referring to the maximum gradient of the phase field variables, so that it can be used as a parameter in numerical criteria.

Since structural relaxations at grain boundaries are on an atomistic scale and should not be considered in mesoscale simulations, the model parameters have discrete values for discrete misorientations and are assumed to be fixed for a given grain configuration. On the other hand, to describe the grain boundary reorientation due to the Herring torque, which occurs on a mesoscale, the free energy and the model parameters are differentiable with respect to inclination dependence.

Test applications show that the theoretically expected grain boundary curvature and velocity are well reproduced for $R/\ell_{gb}>4$ and $\ell_{gb}/\Delta x \approx 10$ and triple junction angles between approximately 100° and 140°, with ℓ_{gb} as the diffuse grain boundary width, R as the mean grain boundary curvature, and Δx as the grid spacing. A higher $\ell_{gb}/\Delta x$ ratio is required (still assuming $R/\ell_{gb}>4$) to resolve triple junctions with larger differences in the grain boundary energies of the intersecting grain boundaries. A similar difficulty in resolving small triple junction angles was experienced for Monte Carlo simulations.[21] One advantage of the proposed phase field methodology compared to Monte Carlo simulation techniques is that depending on the mean grain size, the resolution of the phase field profiles at grain boundaries and triple junctions may be improved by taking a larger diffuse interface width while keeping the grid spacing constant, which requires less computational power. This possibility will be explored in future applications of the model.

Furthermore, expressions (38) and (39) for grain boundary or interface energy can be combined with bulk free energies for different phases and the thin-interface techniques developed for alloys.[29–33,66] In this way, a very general mesoscale modeling approach is obtained to perform efficiently quantitative simulations, 2D and 3D, of phase transformations, diffusion, and coarsening in polycrystalline multiphase and multicomponent structures.

ACKNOWLEDGMENT

N. M. thanks the Research Foundation-Flanders (FWO-Vlaanderen) for financial support.

APPENDIX A: ASYMPTOTIC ANALYSIS

In this appendix, a sharp interface derivation of the grain boundary velocity and the force balance equations at edges and multijunctions is given for the model presented in this paper. We mainly follow the procedures given in Refs. 48, 49, and 61. To be illustrative and simplify the notation, a two-dimensional system is considered. The inclination $\phi_{i,j}=(\nabla\eta_i-\nabla\eta_j)/(|\nabla\eta_i-\nabla\eta_j|)$ then corresponds with a single inclination angle

$$\phi'_{i,j}=\arctan\left(\frac{\nabla_y\eta_i-\nabla_y\eta_j}{\nabla_x\eta_i-\nabla_x\eta_j}\right), \tag{A1}$$

measured with reference to the axis of the x coordinate. The evolution equations for a two-grain system with inclination-dependent grain boundary energy are

$$\frac{\partial\eta_i}{\partial t}=-L_{i,j}\left(m\frac{\partial f_0}{\partial\eta_i}-m\nabla\cdot\left[\frac{\partial\gamma_{i,j}}{\partial\phi'_{i,j}}\frac{\partial\phi'_{i,j}}{\partial(\nabla\eta_i)}\eta_i^2\eta_j^2\right]-\nabla\cdot\left\{\frac{1}{2}\frac{\partial\kappa_{i,j}}{\partial\phi'_{i,j}}\frac{\partial\phi'_{i,j}}{\partial(\nabla\eta_i)}[(\nabla\eta_i)^2+(\nabla\eta_j)^2]+\kappa_{i,j}\nabla\eta_i\right\}\right), \tag{A2a}$$

$$\frac{\partial\eta_j}{\partial t}=-L_{i,j}\left(m\frac{\partial f_0}{\partial\eta_j}-m\nabla\cdot\left[\frac{\partial\gamma_{i,j}}{\partial\phi'_{i,j}}\frac{\partial\phi'_{i,j}}{\partial(\nabla\eta_j)}\eta_i^2\eta_j^2\right]-\nabla\cdot\left\{\frac{1}{2}\frac{\partial\kappa_{i,j}}{\partial\phi'_{i,j}}\frac{\partial\phi'_{i,j}}{\partial(\nabla\eta_j)}[(\nabla\eta_i)^2+(\nabla\eta_j)^2]+\kappa_{i,j}\nabla\eta_j\right\}\right). \tag{A2b}$$

Elaboration of the separate terms in the equation for η_i, using the relations worked out in Appendix B, gives

$$-m\nabla\cdot\left[\frac{\partial\gamma_{i,j}}{\partial\phi'_{i,j}}\frac{\partial\phi'_{i,j}}{\partial(\nabla\eta_i)}\eta_i^2\eta_j^2\right]=-m\left\{\frac{\partial^2\gamma_{i,j}}{\partial\phi'^2_{i,j}}\frac{\eta_i^2\eta_j^2}{|\nabla\eta_i-\nabla\eta_j|^2}(\nabla\phi'_{i,j})\cdot\begin{bmatrix}-(\nabla_y\eta_i-\nabla_y\eta_j)\\ \nabla_x\eta_i-\nabla_x\eta_j\end{bmatrix}\right.$$
$$\left.+\frac{\partial\gamma_{i,j}}{\partial\phi'_{i,j}}\begin{bmatrix}-(\nabla_y\eta_i-\nabla_y\eta_j)\\ \nabla_x\eta_i-\nabla_x\eta_j\end{bmatrix}\cdot\nabla\frac{\eta_i^2\eta_j^2}{|\nabla\eta_i-\nabla\eta_j|^2}\right\}$$
$$=-m\left[\frac{\partial^2\gamma_{i,j}}{\partial\phi'^2_{i,j}}\frac{\eta_i^2\eta_j^2}{|\nabla\eta_i-\nabla\eta_j|}\nabla\cdot\frac{\nabla\eta_i-\nabla\eta_j}{|\nabla\eta_i-\nabla\eta_j|}\right]\quad[+O(1)],\tag{A3}$$

$$-\nabla\cdot\left\{\frac{1}{2}\frac{\partial\kappa'_{i,j}}{\partial\phi'_{i,j}}\frac{\partial\phi'_{i,j}}{\partial(\nabla\eta_i)}[(\nabla\eta_i)^2+(\nabla\eta_j)^2]\right\}=-\frac{1}{2}\left[\frac{\partial^2\kappa_{i,j}}{\partial\phi'^2_{i,j}}\frac{(\nabla\eta_i)^2+(\nabla\eta_j)^2}{|\nabla\eta_i-\nabla\eta_j|^2}(\nabla\phi'_{i,j})\cdot\begin{pmatrix}-\nabla_y\eta_i-\nabla_y\eta_j\\ \nabla_x\eta_i-\nabla_x\eta_j\end{pmatrix}\right.$$
$$\left.+\frac{\partial\kappa_{i,j}}{\partial\phi'_{i,j}}\begin{pmatrix}-(\nabla_y\eta_i-\nabla_y\eta_j)\\ \nabla_x\eta_i-\nabla_x\eta_j\end{pmatrix}\cdot\nabla\frac{(\nabla\eta_i)^2+(\nabla\eta_j)^2}{|\nabla\eta_i-\nabla\eta_j|^2}\right]$$
$$=-\frac{1}{2}\frac{\partial^2\kappa_{i,j}}{\partial\phi'^2_{i,j}}\frac{(\nabla\eta_i)^2+(\nabla\eta_j)^2}{|\nabla\eta_i-\nabla\eta_j|^2}|\nabla\eta_i-\nabla\eta_j|\nabla\cdot\frac{\nabla\eta_i-\nabla\eta_j}{|\nabla\eta_i-\nabla\eta_j|}\quad[+O(1)],\tag{A4}$$

and

$$-\nabla\cdot[\kappa\nabla\eta_i]=-\frac{\partial\kappa_{i,j}}{\partial\phi'^2_{i,j}}\nabla\phi'_{i,j}\cdot\nabla\eta_i-\kappa\nabla^2\eta_i.\tag{A5}$$

Analogous expressions are obtained for η_j except that Eqs. (A3) and (A4) change sign because of the antisymmetric formulation of $\phi_{i,j}$ with respect to η_i and η_j.

If $\kappa_{i,j}(\phi'_{i,j})$ is replaced by $[k_{i,j}(\phi'_{i,j})]^2$, and accordingly $\partial\kappa_{i,j}/\partial\phi'_{i,j}$ by $2k_{i,j}\partial k_{i,j}/\partial\phi'_{i,j}$ and $\partial^2\kappa_{i,j}/\partial\phi'^2_{i,j}$ by $2[(\partial k_{i,j}/\partial\phi_{i,j})'^2+k_{i,j}\partial^2k_{i,j}/\partial\phi'^2_{i,j}]$, expressions (A4) and (A5) resemble the terms in Eq. (27) of Ref. 49 except that there is a dependence of two phase field variables. More specifically, expression (A5) corresponds to the first and second terms on the right-hand side and expression (A4) to the third term. The contributions from these terms to the leading- and first-order solutions of the phase field equations are thus taken from Ref. 49. Contribution (A3), which comes from the inclination dependence of the homogeneous free energy, is not present in the evolution equation for the model discussed in Ref. 49. Applying asymptotic expansions (55)–(58) from Ref. 49, it can be verified that the effects from contribution (A3) on the solution of the phase field equations [this involves multiplication of Eqs. (A3)–(A5) with ϵ^2] are of first and higher order in ϵ, with $\epsilon=\ell_{gb}/R$ as a dimensionless measure for the diffuse interface width and R as the radius of curvature in two dimensions.

Comparison of the different terms in Eqs. (A4) and (A5) with those on the right-hand side of Eq. (27) of Ref. 49 and following the procedure described in Ref. 49 shows that the phase field profiles $\eta_i(r)$ and $\eta_j(r)$ across a diffuse grain boundary satisfy, to leading order, Eqs. (6a), (6b), and (7) derived for a flat grain boundary, with $\kappa_{i,j}=\kappa_{i,j}(\phi'_{i,j})$ and $\gamma_{i,j}=\gamma_{i,j}(\phi'_{i,j})$ constant and x replaced by r, the coordinate along the normal to the grain boundary surface. The same result can be obtained by evaluating Eq. (A2a) and (A2b) for a flat interface. Furthermore, since Eqs. (A3) and (A4) are opposite in sign for η_i and η_j, the integrated Euler equation for the phase field profiles across a grain boundary in equilibrium between two grains gives

$$mf_0+\frac{\kappa_{i,j}}{2}[(\nabla\eta_i)^2+(\nabla\eta_i)^2]-\nabla\eta_i\cdot\frac{\partial}{\partial\nabla\eta_i}\left\{mf_0+\frac{\kappa_{i,j}}{2}[(\nabla\eta_i)^2+(\nabla\eta_i)^2]\right\}-\nabla\eta_j\cdot\frac{\partial}{\partial\nabla\eta_j}\left\{mf_0+\frac{\kappa_{i,j}}{2}[(\nabla\eta_i)^2+(\nabla\eta_i)^2]\right\}$$
$$=mf_0-\frac{\kappa_{i,j}}{2}[(\nabla\eta_i)^2+(\nabla\eta_i)^2]=0,\tag{A6}$$

and, accordingly,

$$\nabla\cdot\frac{\partial}{\partial(\nabla\eta_i)}[mf_0]=\nabla\cdot\frac{\partial}{\partial(\nabla\eta_i)}\left\{\frac{\kappa_{i,j}}{2}[(\nabla\eta_i)^2+(\nabla\eta_i)^2]\right\}.\tag{A7}$$

Considering relations (A6) and (A7) and the fact that $\nabla\cdot\mathbf{r}=\nabla\cdot[(\nabla\eta_i-\nabla\eta_j)/|\nabla\eta_i-\nabla\eta_j|]=1/R$, summation of the solvability conditions for η_i and η_j [Eq. (70) in Ref. 49] gives

$$\frac{v_{gb,n}}{L}\int_0^{+\infty}\left[\left(\frac{\partial\eta_i}{\partial r}\right)^2+\left(\frac{\partial\eta_j}{\partial r}\right)^2\right]dr$$
$$=-\frac{1}{R}\frac{\partial^2\kappa_{i,j}}{\partial\phi'^2_{i,j}}\int_0^{+\infty}\frac{\left(\frac{\partial\eta_i}{\partial r}\right)^2+\left(\frac{\partial\eta_j}{\partial r}\right)^2}{\left(\frac{\partial\eta_i}{\partial r}\right)-\left(\frac{\partial\eta_j}{\partial r}\right)}\left(\frac{\partial\eta_i}{\partial r}-\frac{\partial\eta_j}{\partial r}\right)dr$$
$$-\frac{\partial\kappa_{i,j}}{\partial\phi'_{i,j}}\frac{\partial}{\partial t_1}\int_0^{+\infty}\left[\left(\frac{\partial\eta_i}{\partial r}\right)^2+\left(\frac{\partial\eta_j}{\partial r}\right)^2\right]dr$$
$$-\frac{\kappa_{i,j}}{R}\int_0^{+\infty}\left[\left(\frac{\partial\eta_i}{\partial r}\right)^2+\left(\frac{\partial\eta_j}{\partial r}\right)^2\right]dr,\tag{A8}$$

with t_1 the coordinate tangential to the surface. Evaluation of Eq. (A8) using relations (7), (9), and (12) gives after rearrangement

$$v_{\mathrm{gb},n} = -\frac{L_{i,j}\sqrt{\kappa_{i,j}}}{g(\gamma_{i,j})}\left[\sqrt{\kappa_{i,j}}g(\gamma_{i,j}) + \frac{\partial^2\sqrt{\kappa_{i,j}}g(\gamma_{i,j})}{\partial\phi_{i,j}'^2}\right]\frac{1}{R} \quad \text{(A9)}$$

for the normal velocity of a point on a grain boundary surface. If $\kappa_{i,j}$ and $g^2(\gamma_{i,j})$ have the same inclination-dependent factor as the specific grain boundary energy σ_{gb}, Eq. (A9) simplifies to

$$v_{\mathrm{gb},n} = -L_{i,j}\left(\kappa_{i,j} + \frac{\partial^2\kappa_{i,j}}{\partial\phi_{i,j}'^2}\right)\frac{1}{R}. \quad \text{(A10)}$$

If the inclination dependence of the specific grain boundary energy is completely treated in the gradient contribution in the free energy, $\kappa_{i,j}^2$ must have the same inclination dependence as the specific grain boundary energy and relation (A9) reduces to

$$v_{\mathrm{gb},n} = -L_{i,j}\sqrt{\kappa_{i,j}}\left(\sqrt{\kappa_{i,j}} + \frac{\partial^2\sqrt{\kappa_{i,j}}}{\partial\phi_{i,j}'^2}\right)\frac{1}{R}. \quad \text{(A11)}$$

The latter relation has a form that is very similar to that of Eq. (72) in Ref. 49.

We remark that for nonuniform grain boundary properties, the value of the phase field variables at the middle of the interface is no longer constant along the grain boundary, as it varies with $\gamma_{i,j}(\phi_{i,j})$. Therefore, the gradients of the phase fields $\nabla\eta_i$ and $\nabla\eta_j$ have a component along the tangential to the surface, although the vector $(\nabla\eta_i - \nabla\eta_j)/|\nabla\eta_i - \nabla\eta_j|$ is always perpendicular to the surface. The tangential components are omitted in Eq. (A8) since their contributions vanish after summation of the equations for η_i and η_j or are of two orders higher in ϵ than the other terms (see explanation at the end of Appendix B).

Following the procedure described in Refs. 48 and 61, the force of a diffuse grain boundary acting on a plane that cuts its surface can be calculated in the sharp interface limit. Assume, for instance, a grain boundary surface with normal $\mathbf{r}$ as in Fig. 1(b) and a plane cutting the surface oriented perpendicularly to it with normal $\mathbf{t}_1$ and so that direction $\mathbf{t}_2$ is common to the grain boundary surface and the plane. The local force acting on the plane is given by

$$F = \Xi\cdot\mathbf{t}_1, \quad \text{(A12)}$$

with Ξ as a tensor with, for the current model, the elements

$$\Xi_{pq} = \nabla_p\eta_i\frac{\partial f}{\partial(\nabla_q\eta_i)} + \nabla_q\eta_j\frac{\partial f}{\partial(\nabla_q\eta_j)} - \delta_{pq}f, \quad \text{(A13)}$$

where p,q run over the spatial coordinates, or in tensor notation

$$\Xi = \nabla\eta_i\otimes\frac{\partial f}{\partial\nabla\eta_i} + \nabla\eta_j\otimes\frac{\partial f}{\partial\nabla\eta_j} - f\mathbf{I}, \quad \text{(A14)}$$

with $\mathbf{I}$ as the unit tensor. Assuming $\ell_{\mathrm{gb}} \ll R_1$ and R_2 infinite and using Eq. (7), we obtain to leading order

$$\frac{\partial f}{\partial(\nabla\eta_i)} = \frac{\partial\kappa_{i,j}}{\partial\alpha_1}\frac{\left(\frac{\partial\eta_i}{\partial r}\right)^2 + \left(\frac{\partial\eta_j}{\partial r}\right)^2}{\left|\frac{\partial\eta_i}{\partial r} - \frac{\partial\eta_j}{\partial r}\right|}\mathbf{t}_1 + \kappa_{i,j}\frac{\partial\eta_i}{\partial r}\mathbf{r}, \quad \text{(A15)}$$

with the angle α_1 measured in the curvilinear coordinate system. By consequence, in a single point

$$\Xi = \left[\left(\frac{\partial\eta_i}{\partial r}\right)^2 + \left(\frac{\partial\eta_j}{\partial r}\right)^2\right]\left[\mathbf{r}\otimes\left(\frac{\partial\kappa_{i,j}}{\partial\alpha_1}\mathbf{t}_1 + \kappa_{i,j}\mathbf{r}\right) - \kappa_{i,j}\mathbf{I}\right], \quad \text{(A16)}$$

and

$$F = \Xi\cdot\mathbf{t}_1 = \left[\left(\frac{\partial\eta_i}{\partial r}\right)^2 + \left(\frac{\partial\eta_j}{\partial r}\right)^2\right]\left(\frac{\partial\kappa_{i,j}}{\partial\alpha_1}\mathbf{r} - \kappa_{i,j}\mathbf{t}_1\right). \quad \text{(A17)}$$

Integration of Eq. (A17) along the phase field profiles across a diffuse grain boundary gives the total force acting on the plane per unit length (with the length measured along direction $\mathbf{t}_2$) as

$$\begin{aligned} f &= \int_0^\infty F dr = \frac{\partial}{\partial\alpha_1}\left\{\kappa_{i,j}\int_0^\infty\left[\left(\frac{\partial\eta_i}{\partial r}\right)^2 + \left(\frac{\partial\eta_j}{\partial r}\right)^2\right]dr\right\}\mathbf{r} \\ &\quad - \kappa_{i,j}\left\{\int_0^\infty\left[\left(\frac{\partial\eta_i}{\partial r}\right)^2 + \left(\frac{\partial\eta_j}{\partial r}\right)^2\right]dr\right\}\mathbf{t}_1 \\ &= \frac{\partial\sigma_{\mathrm{gb}}}{\partial\alpha_1}\mathbf{r} - \sigma_{\mathrm{gb}}\mathbf{t}_1, \end{aligned} \quad \text{(A18)}$$

where relations (7), (9), and (12) are used to evaluate the integral.

APPENDIX B: VECTOR RELATIONS AND EXPANSIONS

Consider the angle

$$\phi_{i,j}' = \arctan\left(\frac{\nabla_y\eta_i - \nabla_y\eta_j}{\nabla_x\eta_i - \nabla_x\eta_j}\right), \quad \text{(B1)}$$

measured with reference to the axis of the x coordinate. It can then be verified that (see also Ref. 49)

$$\frac{\partial\phi_{i,j}'}{\partial\nabla\eta_i} = -\frac{\partial\phi_{i,j}'}{\partial\nabla\eta_j} = \frac{1}{|\nabla\eta_i - \nabla\eta_j|^2}\begin{bmatrix} -(\nabla_y\eta_i - \nabla_y\eta_j) \\ \nabla_x\eta_i - \nabla_x\eta_j \end{bmatrix}, \quad \text{(B2)}$$

is a vector tangential to the surface. Furthermore,

$$\begin{aligned} -(\nabla\eta_i - \nabla\eta_j)\cdot\frac{\partial\phi_{i,j}'}{\partial(\nabla\eta_i)} &= -\frac{1}{|\nabla\eta_i - \nabla\eta_j|^2} \\ &\quad\times\left\{(\nabla_x\eta_i - \nabla_x\eta_j\nabla_y\eta_i - \nabla_y\eta_j)\right. \\ &\quad\left.\cdot\begin{bmatrix} -(\nabla_y\eta_i - \nabla_y\eta_j) \\ \nabla_x\eta_i - \nabla_x\eta_j \end{bmatrix}\right\} = 0, \end{aligned} \quad \text{(B3)}$$

$$\nabla \cdot \left[|\nabla \eta_i - \nabla \eta_j|^2 \frac{\partial \phi'_{i,j}}{\partial(\nabla \eta_i)} \right] = \nabla \cdot \left[|\nabla \eta_i - \nabla \eta_j|^2 \frac{\partial \phi'_{i,j}}{\partial(\nabla \eta_j)} \right] = 0, \tag{B4}$$

and

$$(\nabla \phi'_{i,j}) \cdot \begin{bmatrix} -(\nabla_y \eta_i - \nabla_y \eta_j) \\ \nabla_x \eta_i - \nabla_x \eta_j \end{bmatrix} = |\nabla \eta_i - \nabla \eta_j| \nabla \cdot \frac{\nabla \eta_i - \nabla \eta_j}{|\nabla \eta_i - \nabla \eta_j|}. \tag{B5}$$

With $\mathbf{r}$ the normal to the grain boundary surface and $\mathbf{r}'$ directed along the gradient of η_i, it can be derived that

$$\nabla \left[\frac{1}{|\nabla \eta_i - \nabla \eta_j|} \right] = \left(\frac{\nabla \eta_i - \nabla \eta_j}{|\nabla \eta_i - \nabla \eta_j|} \right) (\nabla^2 \eta_i - \nabla^2 \eta_j) = (\nabla^2 \eta_i - \nabla^2 \eta_j)\mathbf{r} \tag{B6}$$

is directed along the normal to the surface and

$$\begin{aligned} \nabla (\nabla \eta_i)^2 &= \nabla \left(\frac{\partial \eta_i}{\partial r} \mathbf{r}' \right)^2 \\ &= 2 \left(\frac{\partial \eta_i}{\partial r} \mathbf{r}' \right) \left[\nabla \cdot \left(\frac{\partial \eta_i}{\partial r} \mathbf{r}' \right) \right] \\ &= 2(\nabla \eta_i)(\nabla^2 \eta_i) \end{aligned} \tag{B7}$$

$$= 2 \left(\frac{\partial \eta_i}{\partial r} \mathbf{r} \right) (\nabla^2 \eta_i) + \left(\frac{\partial \eta_i}{\partial t_1} \mathbf{t}_1 \right) (\nabla^2 \eta_i), \tag{B8}$$

has a contribution along the tangential, which is of one order higher in ϵ than the radial term $[\partial \eta_i / \partial t_1 = O(1),\ \partial \eta_i / \partial r = O(1/\epsilon)]$. Since the vector $[-(\nabla_y \eta_i - \nabla_y \eta_j) \quad (\nabla_x \eta_i - \nabla_x \eta_j)]$ is directed along the tangential to the surface, the second term in Eqs. (A3) and (A4) gives a contribution for curved surfaces and $\gamma_{i,j}$ inclination dependent, which is of the order $O(1)$ in ϵ. Moreover, the contributions in $(\partial \eta_i / \partial t_1)^2$ and $(\partial \eta_j / \partial t_1)^2$ in

$$[(\nabla \eta_i)^2 + (\nabla \eta_j)^2] = \left[\left(\frac{\partial \eta_i}{\partial r} \right)^2 + \left(\frac{\partial \eta_i}{\partial t_1} \right)^2 + \left(\frac{\partial \eta_j}{\partial r} \right)^2 + \left(\frac{\partial \eta_j}{\partial t_1} \right)^2 \right] \tag{B9}$$

$$= \left[\left(\frac{\partial \eta_i}{\partial r} \right)^2 + \left(\frac{\partial \eta_j}{\partial r} \right)^2 \right] + O(1), \tag{B10}$$

are of two orders higher in ϵ than those in $(\partial \eta_i / \partial r)^2$ and $(\partial \eta_j / \partial r)^2$.

*nele.moelans@mtm.kuleuven.be

[1] M. Furtkamp, G. Gottstein, D. A. Molodov, V. N. Semenov, and L. S. Shvindlerman, Acta Mater. **46**, 4103 (1998).
[2] M. Upmanyu, G. Hassold, A. Kazaryan, E. Holm, Y. Wang, B. Patton, and D. Srolovitz, Interface Sci. **10**, 201 (2002).
[3] K. Janssens, D. Olmstead, E. A. Holm, S. Foiles, S. Plimpton, and P. Derlet, Nat. Mater. **5**, 124 (2006).
[4] S. Foiles and J. Hoyt, Acta Mater. **54**, 3351 (2006).
[5] F. J. Humphreys and M. Hatherly, *Recrystallization and Related Annealing Phenomena* (Pergamon, Oxford, 1996).
[6] D. Fan, C. Geng, and L.-Q. Chen, Acta Mater. **45**, 1115 (1997).
[7] C. E. Krill III and L.-Q. Chen, Acta Mater. **50**, 3057 (2002).
[8] S. G. Kim, D. I. Kim, W. T. Kim, and Y. B. Park, Phys. Rev. E **74**, 061605 (2006).
[9] D. Zöllner and P. Streitenberger, Scr. Mater. **54**, 1697 (2006).
[10] M. Miodownik, E. A. Holm, and G. N. Hassold, Scr. Mater. **42**, 1173 (2000).
[11] D. Fan, L.-Q. Chen, and S.-P. P. Shen, J. Am. Ceram. Soc. **81**, 526 (1998).
[12] N. Moelans, B. Blanpain, and P. Wollants, Acta Mater. **54**, 1175 (2006).
[13] Y. Suwa, Y. Saito, and H. Onodera, Scr. Mater. **55**, 407 (2006).
[14] N. Moelans, B. Blanpain, and P. Wollants, Acta Mater. **55**, 2173 (2007).
[15] Y. Suwa, Y. Saito, and H. Onodera, Acta Mater. **55**, 6881 (2007).
[16] E. Holm, G. Hassold, and M. Miodownik, Acta Mater. **49**, 2981 (2001).
[17] G. Rohrer, Annu. Rev. Mater. Res. **35**, 99 (2005).
[18] A. Kazaryan, B. Patton, S. Dregia, and Y. Wang, Acta Mater. **50**, 499 (2002).
[19] Y. Suwa, Y. Saito, and H. Onodera, Comput. Mater. Sci. **40**, 40 (2007).
[20] F. Humphreys, Acta Mater. **45**, 4231 (1997).
[21] E. Holm, M. Miodownik, and A. Rollett, Acta Mater. **51**, 2701 (2003).
[22] L.-Q. Chen, Annu. Rev. Mater. Res. **32**, 113 (2002).
[23] W. J. Boettinger, J. A. Warren, C. Beckermann, and A. Karma, Annu. Rev. Mater. Res. **32**, 163 (2002).
[24] N. Moelans, B. Blanpain, and P. Wollants, CALPHAD: Comput. Coupling Phase Diagrams Thermochem. **32**, 268 (2008).
[25] J. Cahn and J. Hilliard, J. Chem. Phys. **28**, 258 (1958).
[26] D. Fan and L.-Q. Chen, Acta Mater. **45**, 611 (1997).
[27] A. A. Wheeler, W. J. Boettinger, and G. B. McFadden, Phys. Rev. E **47**, 1893 (1993).
[28] A. Karma and W.-J. Rappel, Phys. Rev. E **53**, R3017 (1996).
[29] J. Tiaden, B. Nestler, H. Diepers, and I. Steinbach, Physica D **115**, 73 (1998).
[30] S. G. Kim, W. T. Kim, and T. Suzuki, Phys. Rev. E **60**, 7186 (1999).
[31] A. Karma, Phys. Rev. Lett. **87**, 115701 (2001).
[32] B. Echebarria, R. Folch, A. Karma, and M. Plapp, Phys. Rev. E **70**, 061604 (2004).
[33] R. Folch and M. Plapp, Phys. Rev. E **72**, 011602 (2005).
[34] A. Kazaryan, Y. Wang, S. Dregia, and B. Patton, Acta Mater. **50**, 2491 (2002).
[35] N. Ma, Q. Chen, and Y. Wang, Scr. Mater. **54**, 1919 (2006).
[36] N. Moelans, B. Blanpain, and P. Wollants, Phys. Rev. Lett. **101**, 025502 (2008).
[37] N. Moelans and F. Spaepen (unpublished).
[38] L.-Q. Chen and W. Yang, Phys. Rev. B **50**, 15752 (1994).

[39] L.-Q. Chen, Scr. Metall. Mater. **32**, 115 (1995).
[40] A. Kazaryan, Y. Wang, S. A. Dregia, and B. R. Patton, Phys. Rev. B **61**, 14275 (2000).
[41] R. Weinstock, *Calculus of Variations* (McGraw-Hill, New York, 1952), Chap. 3, pp. 16–26.
[42] E. W. Weisstein, Euler-Lagrange Differential Equation, from MathWorld–A Wolfram Web Resource (http://mathworld.wolfram.com/Euler-LagrangeDifferentialEquation.html).
[43] N. Ma, A. Kazaryan, S. Dregia, and Y. Wang, Acta Mater. **52**, 3869 (2004).
[44] Y. Suwa and Y. Saito, Mater. Trans. **46**, 1208 (2005).
[45] S. Allen and J. Cahn, Acta Metall. **27**, 1085 (1979).
[46] D. Fan and L.-Q. Chen, Philos. Mag. Lett. **75**, 187 (1997).
[47] A. Wheeler and G. McFadden, Eur. J. Appl. Math. **7**, 367 (1996).
[48] A. Wheeler and G. McFadden Proc. R. Soc. London, Ser. A **453**, 1611 (1997).
[49] G. B. McFadden, A. A. Wheeler, R. J. Braun, S. R. Coriell, and R. F. Sekerka, Phys. Rev. E **48**, 2016 (1993).
[50] A. Kazaryan, Y. Wang, S. A. Dregia, and B. R. Patton, Phys. Rev. B **63**, 184102 (2001).
[51] The procedure has been implemented using MATLAB (N. Moelans, 2007).
[52] J. Cahn and D. Hoffman, Acta Metall. **22**, 1205 (1974).
[53] C. Herring, in *The Physics of Powder Metallurgy*, edited by W. E. Kingston (McGraw-Hill, New York, 1951).
[54] C. Herring, Phys. Rev. **82**, 87 (1951).
[55] J. Eggleston, G. McFadden, and P. Voorhees, Physica D **150**, 91 (2001).
[56] J. M. Debierre, A. Karma, F. Celestini, and R. Guerin, Phys. Rev. E **68**, 041604 (2003).
[57] I. Loginova, J. Ågren, and G. Amberg, Acta Mater. **52**, 4055 (2004).
[58] A. Karma and W.-J. Rappel, Phys. Rev. E **57**, 4323 (1998).
[59] T. Haxhimali, A. Karma, F. Gonzales, and M. Rappaz, Nat. Mater. **5**, 660 (2006).
[60] D. Hoffman and J. Cahn, Surf. Sci. **31**, 368 (1972).
[61] B. Nestler and A. A. Wheeler, Phys. Rev. E **57**, 2602 (1998).
[62] S. De Groot and P. Mazur, *Non-Equilibrium Thermodynamics*, 1st ed. (North-Holland, Amsterdam, 1963).
[63] N. Moelans, F. Wendler, and B. Nestler (unpublished).
[64] I. Steinbach and F. Pezzolla, Physica D **134**, 385 (1999).
[65] H. Garcke, B. Nestler, and B. Stinner, SIAM J. Appl. Math. **64**, 775 (2004).
[66] J. Eiken, B. Bottger, and I. Steinbach, Phys. Rev. E **73**, 066122 (2006).